Mesoscale Processes Driving Offshore MCS Initiation in the South Asian Summer Monsoon: Insights from an Ensemble-Based Satellite Data Assimilation Experiment

CHIN-HSUAN PENG[a] AND XINGCHAO CHEN[a]

[a] *Department of Meteorology and Atmospheric Science, and Center for Advanced Data Assimilation and Predictability Techniques, The Pennsylvania State University, University Park, Pennsylvania*

(Manuscript received 8 November 2024, in final form 28 February 2025, accepted 10 April 2025)

ABSTRACT: Mesoscale convective systems (MCSs) are the primary rainfall contributors over the Bay of Bengal (BoB) during the South Asian summer monsoon. Previous studies have established a strong connection between MCS initiation over the BoB and diurnal gravity waves propagating from India. However, the precise role these waves play in triggering offshore MCSs remains unquantified. In this study, we analyze a typical MCS event, representative of the climatological spatiotemporal characteristics of MCS initiation in the region, to investigate the relative roles of diurnal gravity waves and other mesoscale processes in offshore MCS initiation. An ensemble-based satellite data assimilation (DA) experiment is conducted, assimilating all-sky infrared radiances from *Meteosat-8* into the Weather Research and Forecasting (WRF) Model. The ensemble forecast, initialized from DA analyses, shows that many ensemble members accurately capture both the timing and location of MCS initiation. The analysis of the "successful" members reveals diurnal gravity waves play a significant role in enhancing lower-tropospheric moisture and destabilizing the offshore environment. Surprisingly, similar gravity waves and destabilization are also present in members that failed to capture MCS initiation. Further analysis indicates that land-breeze front from northern Sri Lanka is a key factor distinguishing successful from "unsuccessful" members, which, in successful members, is strong enough to lift air above the level of free convection (LFC) and lead to MCS initiation. Accurately simulating the land-breeze front depends on the correct representation of pre-MCS clouds and surface winds. This suggests that while diurnal gravity waves contribute to environmental destabilization, surface and boundary layer processes are crucial for the practical predictability of offshore MCS initiation.

SIGNIFICANCE STATEMENT: The majority of summer monsoon rainfall over the Bay of Bengal is attributed to large and long-lasting thunderstorms. Scientists hypothesized atmospheric waves from India play a role in the initiation of these thunderstorms, but the role has not been quantified yet. Therefore, we study a typical thunderstorm using satellite data and computer models. The results show that atmospheric waves from India create an environment that is favorable for thunderstorm formation. However, the favorable environment alone does not guarantee thunderstorm initiation. A key thunderstorm-triggering process is the land breeze from northern Sri Lanka. Accurately simulating the land breeze depends on correctly simulating prestorm clouds and near-surface winds. Assimilation of satellite observations can improve the forecast of thunderstorm initiation.

KEYWORDS: Gravity waves; Mesoscale processes; Mesoscale forecasting; Data assimilation; Diurnal effects; Convection

1. Introduction

Diurnal offshore rainfall propagation is a prevalent phenomenon observed across many tropical coastal regions, facilitated by weak Coriolis forces and abundant moisture (e.g., Rotunno 1983; Fang and Du 2022). Previous observational and modeling studies have associated this phenomenon with offshore land breezes (e.g., Chen et al. 2014, 2015, 2016, 2017; Wang et al. 2024; Wapler and Lane 2012; Bai et al. 2021; Natoli and Maloney 2023) and/or diurnal gravity waves (e.g., Jiang 2012a,b; Mapes et al. 2003; Ruppert et al. 2020; Ruppert and Zhang 2019; Qian et al. 2009; Chen and Du 2024; Hu and Chen 2025). Both gravity waves and land–sea breeze are components of diurnal land–sea circulation driven by land–sea thermal contrast. Diurnal gravity waves represent the linear response to this thermal forcing, while the land–sea breeze manifests as a nonlinear component of the circulation. Of all tropical coasts, the Indian east coast exhibits the most pronounced diurnal offshore rainfall propagation (Fang and Du 2022). During the summer monsoon season (June–September), long-range diurnal rainfall propagation is frequently observed from the Indian east coast to the Bay of Bengal (BoB), driven by strong southwesterly monsoonal winds and favorable thermodynamic conditions. This often results in a characteristic afternoon rainfall peak at the center of the BoB (Peng and Chen 2023).

The diurnal convection/rainfall propagation over the BoB was first investigated by Yang and Slingo (2001) using long-term satellite brightness temperature observations (OBSs). Their seminal study revealed a diurnal deep convection propagation from the Indian east coast toward the BoB, spanning from early morning to afternoon. Following this work, several statistical studies have identified similar convection/rainfall propagation patterns (e.g., Li and Carbone 2015; Liu et al. 2008; Zuidema 2003). Based on the observed high propagation speeds (~15–20 m s^{-1}), these studies hypothesized that diurnal gravity waves, originating from inland India, play a

Corresponding author: Xingchao Chen, xzc55@psu.edu

DOI: 10.1175/JAS-D-24-0231.1

key role in driving the phenomenon. Additionally, satellite observations have shown that most monsoonal precipitation over the BoB is associated with large cloud systems containing extensive stratiform regions embedded with deep convective cores (e.g., Chen et al. 2017; Romatschke et al. 2010; Zipser et al. 2006). This suggests that mesoscale convective systems (MCSs) might be important contributing systems to the diurnal rainfall cycle over the BoB during the monsoon season. Therefore, understanding the initiation and evolution of MCSs is crucial for explaining the physical mechanisms behind diurnal rainfall propagation in this region.

Using 20 years of satellite observations and cloud tracking/classification, Peng and Chen (2023) quantified the contributions of different convective systems, such as shallow, deep, and MCS convection, to the BoB rainfall diurnal cycle. They found that MCSs contribute ~75% of the BoB rainfall during the summer monsoon season. In addition, they identified a pronounced diurnal offshore-propagating MCS initiation frequency maximum, originating from the eastern coast of India, plays an important role in shaping the diurnal cycle pattern over the BoB. Global reanalyses indicated a strong correlation between the offshore-propagating MCS initiation frequency maxima and diurnal low-level wind perturbations, suggesting the potential role of gravity waves in triggering MCSs. In a subsequent study (Peng and Chen 2024), they developed a two-dimensional linear model that can be driven by realistic meteorological fields from reanalyses. Using the linear model, they confirmed that the observed offshore-propagating MCS initiation frequency maxima is consistent with the propagation of diurnal gravity waves emitted from the Indian coastline, and they hypothesized that these waves may enhance the offshore atmospheric instability and create favorable conditions for MCS initiation. Furthermore, they showed that abundant moisture, particularly in the lower troposphere, is essential for the initiation of offshore MCSs.

However, in both Peng and Chen (2023, 2024) and earlier studies, the role of diurnal gravity waves in offshore MCS initiation has been inferred from the consistent propagation patterns of these waves and the initiation frequency and/or rainfall of MCSs. The exact physical mechanism by which diurnal gravity waves trigger offshore MCSs has yet to be quantified. Additionally, accurately simulating the diurnal cycles of convection and precipitation over the BoB remains a challenge for both regional and global models (e.g., Chan et al. 2022; Dai and Trenberth 2004; Dirmeyer et al. 2012). Peng and Chen (2024) suggested that diurnal gravity waves emitted from the eastern coasts of India during the monsoon season have a characteristic wavelength of slightly longer than 1000 km, driven by the diurnal land–sea thermal contrast. In theory, models should be capable of capturing such low-frequency (i.e., diurnal) and long-wavelength fundamental waves. So why do numerical models struggle to accurately simulate the diurnal cycle of convection in this region?

The objective of this research is to deepen our understanding of the role of diurnal gravity waves and other potential processes in offshore monsoonal MCS initiation over the BoB. To achieve this, we select a representative MCS case that aligns with the climatological spatiotemporal characteristics of MCS initiation in the study region (Peng and Chen 2023, 2024). We then employ ensemble-based satellite all-sky infrared radiance data assimilation (DA) techniques to generate an ensemble forecast for this MCS case. By analyzing the performances of different representative ensemble members, this study aims to address the following key questions:

1) What is the precise role of diurnal gravity waves in offshore MCS initiation? What other processes interact with diurnal gravity waves to decide the location and timing of MCS initiation?
2) How do these processes influence the practical predictability (i.e., the different prediction skills across ensemble members) of offshore MCS initiation?

The rest of this research is organized as follows. Section 2 provides an overview of the typical MCS case. The DA system and experimental design are introduced in section 3. In section 4, we examine the role of diurnal gravity waves in the MCS initiation. Other mesoscale processes contributing to the MCS initiation are analyzed in section 5. Finally, section 6 presents the conclusions, discussion, and suggestions for future research.

2. MCS case overview

As demonstrated in Peng and Chen (2024), the global MCS dataset from Feng et al. (2021) reveals a distinct diurnal propagation pattern in the frequency of MCS initiation within ~400 km of the east coast of India. This diurnal signal originates near the coastline around 0000 LST and propagates offshore, reaching ~400 km from the coast over the following few hours (see Fig. 3 in their paper). MCSs initiate frequently along this diurnal propagation path. The mean propagation speed of the diurnal MCS initiation frequency signal is approximately 19 m s^{-1}, which aligns with the speed of offshore-propagating diurnal gravity waves. To illustrate this climatological feature, a representative MCS event, initiated over the offshore region of the Indian east coast on 5 July 2018, is selected for investigation. The MCS initiated at ~11.25°N, 82.10°E (approximately 200 km off the coast) around 0500 LST (Figs. 1a,b). Consistent with Peng and Chen (2024), the initiation time of the MCS is defined as the first detection of a cold-cloud top (brightness temperature < 241 K). Both the location and timing of this MCS event align closely with the offshore-propagating MCS initiation frequency pattern described by Peng and Chen (2024). Following initiation, an upscale growth of convection can be observed between 0500 and 0900 LST (Figs. 1b–d). While the physical mechanisms behind this upscale growth also merit further investigation, this study focuses on the physical processes leading to the convective initiation of the MCS event. Nonetheless, potential processes influencing the upscale growth of the MCS will be discussed in section 6.

Figure 2 shows the fifth major global reanalysis produced by the European Centre for Medium-Range Weather Forecasts (ECMWF) (ERA5) environmental conditions leading up to the initiation of the MCS event. The fields shown are averaged over 1–6 h preceding the event's initiation (i.e., from

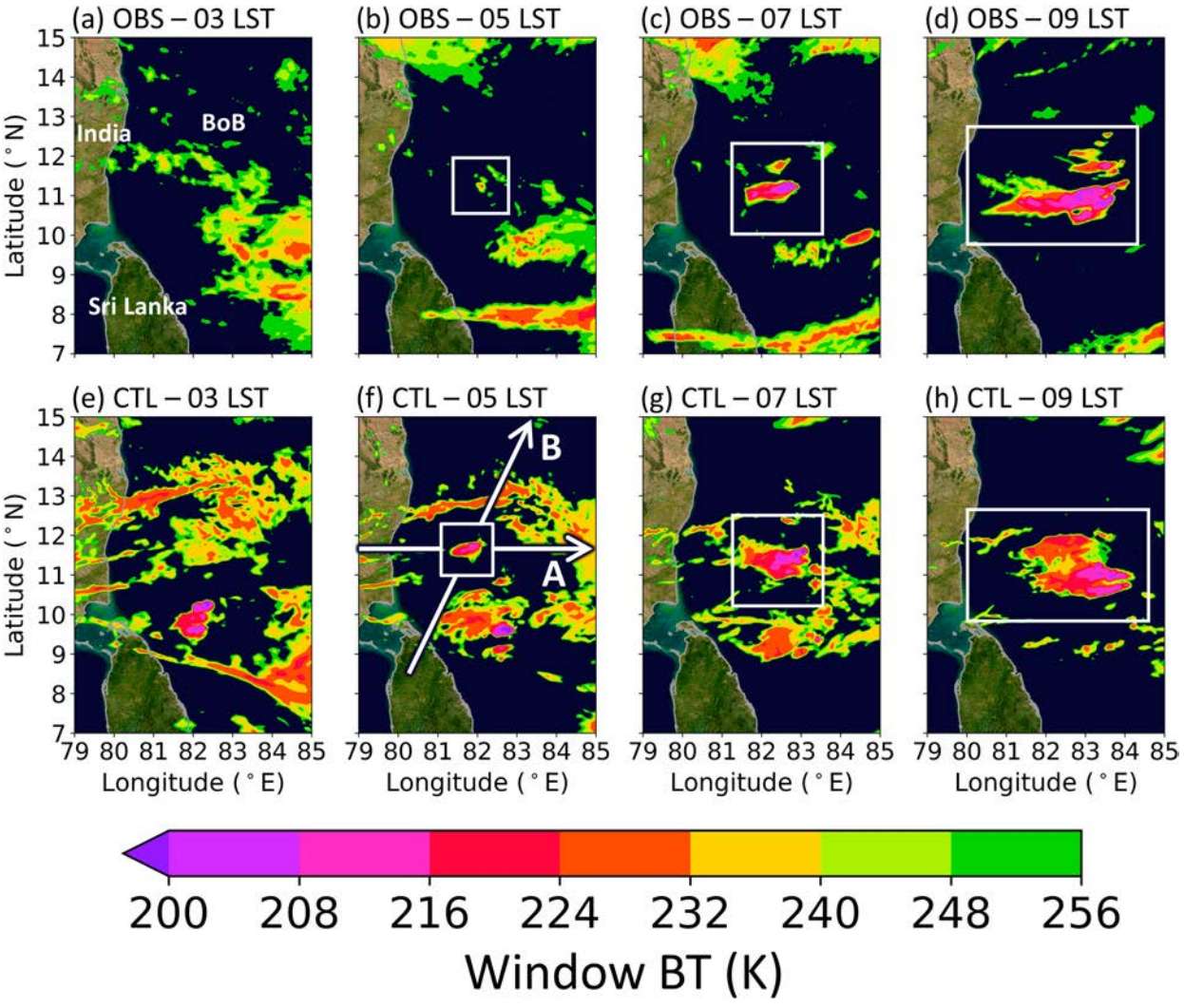

FIG. 1. Plan views of window channel BTs near the east coasts of India and Sri Lanka from *Meteosat-8* OBSs at (a) 0300, (b) 0500, (c) 0700, and (d) 0900 LST. (e)–(h) As in (a)–(d), but from the CTL member. The MCS of interest is located within the white boxes. White arrows A and B in (f) represent the cross sections from India and northern Sri Lanka through the MCS initiation location.

2300 LST 4 July to 0400 LST 5 July). The environment over the BoB appears highly conducive to MCS initiation, consistent with the climatology of the summer monsoon season (e.g., Chen et al. 2018; Peng and Chen 2023). During the summer monsoon, the Tibetan Plateau functions as a key elevated diabatic heating source, creating a thermal low in the lower- to midtroposphere and an upper-tropospheric South Asia (Tibetan) high to the north of the BoB. This setup induces low-level southwesterly monsoon winds (Figs. 2a,b) and an upper-level easterly jet (Fig. 2c) over the BoB. The low-level monsoon winds, which originate from the south Indian Ocean, carry significant moisture evaporated from the tropical ocean surface and transport it to the BoB. As a result, high convective available potential energy (CAPE) and total column water vapor (TCWV) are observed over the BoB (Figs. 2a,b). In addition, the sharp tropospheric temperature gradient between the Tibetan Plateau and the BoB generates a pronounced deep-layer shear between 400 hPa and the surface (Fig. 2c). Previous studies have suggested that, in tropical regions, stronger environmental deep-layer shear can contribute to more organized and intense MCSs (Chen et al. 2023).

3. Data and methodology

a. Data assimilation system

The Pennsylvania State University ensemble Kalman filter (PSU-EnKF) system is employed to generate a high-resolution initial ensemble analysis for the MCS event. This system is mainly composed of an EnKF (Evensen 1994) and a regional convection-permitting numerical model. The observation operator used for satellite all-sky infrared brightness temperature (BT) assimilation is the Community Radiative Transfer Model (CRTM; Ding et al. 2011), and the forecast model used for the

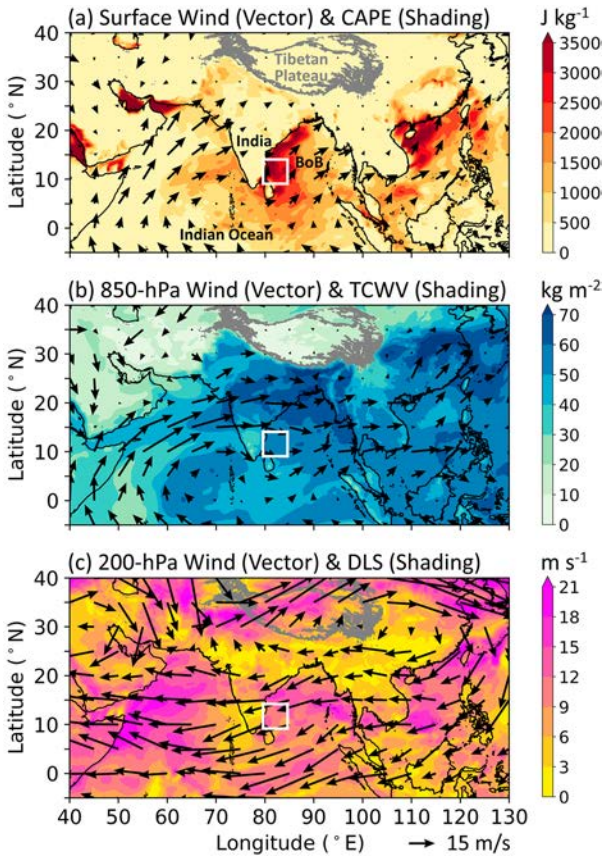

FIG. 2. Spatial distributions of (a) surface winds and convective available potential energy (CAPE), (b) 850-hPa winds and total column water vapor (TCWV), and (c) 200-hPa winds and deep-layer shear (DLS) averaged between 1 and 6 h before the MCS initiation (2300 LST 4 Jul–0400 LST 5 Jul; initiation location is indicated by the white boxes). DLS is measured by calculating the wind differences between 400- and 1000-hPa layers. The Tibetan Plateau is enclosed by the gray contour of 4000-m height.

study is the Advanced Research version of WRF (WRF-ARW, version 4.4.2; Skamarock et al. 2019) Model.

In the PSU-EnKF system, information from observation and background model forecast are combined to create an improved initial condition. This goal can be achieved by the following EnKF update equation (i.e., analysis step):

$$\mathbf{x}_{a,k} = \mathbf{x}_{b,k} + \mathbf{P}_b\mathbf{H}^{\mathrm{T}}(\mathbf{H}\mathbf{P}_b\mathbf{H}^{\mathrm{T}} + \mathbf{R})^{-1}(\mathbf{y}_o - \mathbf{H}\mathbf{x}_{b,k}). \quad (1)$$

The equation calculates a posterior estimate of model state variables $\mathbf{x}_{a,k}$ (also known as the "analysis") by updating a prior estimate $\mathbf{x}_{b,k}$ (also known as the "background" from previous forecast) using the information from observations $\mathbf{y}_o$. The $\mathbf{H}$ is an observation operator that translates $\mathbf{x}_{b,k}$ into observation space for direct comparison with $\mathbf{y}_o$ and calculates innovations ($\mathbf{y}_o - \mathbf{H}\mathbf{x}_{b,k}$); $\mathbf{P}_b$ is the background error covariance calculated from the model ensemble forecasts, which is used to estimate the model forecast uncertainty and the correlations between different model state variables; $\mathbf{R}$ represents the observation error covariance; and $\mathbf{P}_b\mathbf{H}^{\mathrm{T}}(\mathbf{H}\mathbf{P}_b\mathbf{H}^{\mathrm{T}} + \mathbf{R})^{-1}$ in total

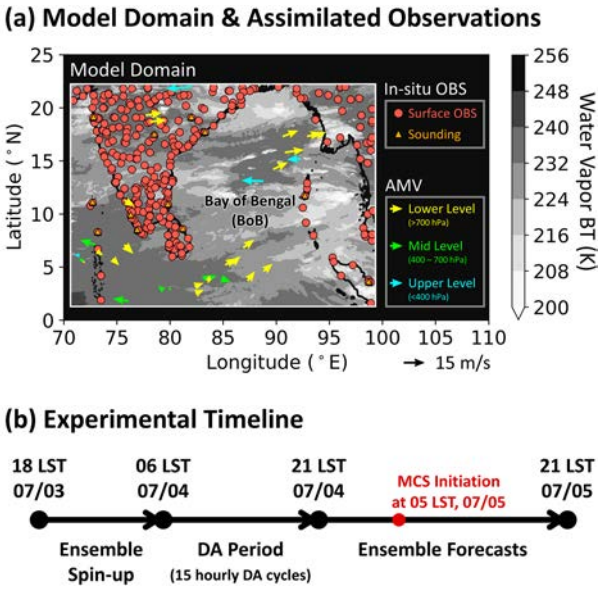

FIG. 3. (a) Model domain and assimilated OBSs and (b) the timeline of DA experiment and ensemble forecast. The assimilated OBSs include in situ OBSs, AMVs, and water vapor BTs.

is called Kalman gain, which can weigh the information from the calculated innovations and propagate the weighted information from observation space back to model state space. To avoid the potential "filter divergence" (Houtekamer and Zhang 2016), we apply 80% relaxation to prior perturbations (Zhang et al. 2004) after the analysis step, following our previous studies (Chan and Chen 2022; Chan et al. 2022; Hartman et al. 2023).

After each analysis step, an updated ensemble analysis is generated, which serves as the basis for initializing a short-term WRF ensemble forecast. This forecast produces the background state $\mathbf{x}_{b,k}$ and background error covariance $\mathbf{P}_b$ for the next analysis step. This process, known as the "forecast step," together with the analysis step, completes a single DA cycle. These DA cycles will be repeated throughout the entire DA period. The objective is to generate improved high-resolution initial conditions for the ensemble forecast of the MCS event. The detailed experimental design is presented in the following section.

b. *Experimental design*

The experiments employ a single WRF domain consisting of 800 × 600 grid points with a 4-km grid spacing, centered on the MCS initiation location (Fig. 3a). Forty-five stretched vertical model levels[1] are used, with enhanced resolution in the boundary layer and a model top at 20 hPa. The model physics schemes include the WRF double-moment 6-class (WDM6)

[1] The 45 eta levels are 1.000, 0.993, 0.983, 0.970, 0.955, 0.937, 0.917, 0.894, 0.869, 0.842, 0.814, 0.783, 0.752, 0.719, 0.685, 0.651, 0.616, 0.581, 0.545, 0.510, 0.475, 0.441, 0.407, 0.374, 0.341, 0.310, 0.280, 0.251, 0.223, 0.197, 0.172, 0.149, 0.127, 0.107, 0.089, 0.073, 0.060, 0.048, 0.037, 0.028, 0.021, 0.014, 0.009, 0.004, and 0.000.

microphysics scheme (Lim and Hong 2010), the Rapid Radiative Transfer Model for Global Climate Model (RRTMG) for longwave (LW) radiation (Iacono et al. 2008), the new Goddard scheme for shortwave radiation (Chou and Suarez 1999), the unified Noah land surface scheme (Tewari et al. 2004), and the Yonsei University (YSU) boundary layer scheme (Hong et al. 2006). No cumulus scheme is used in the experiments.

The design of the DA experiment and ensemble forecast is shown in Figs. 3a and 3b. The experiment consists of 50-member ensemble simulations, initiated at 1800 LST 3 July 2018. To construct the 50-member initial fields, we use ERA5 (Hersbach et al. 2020) data at 1800 LST 3 July, along with the ERA5 10-member ensemble fields from 1800 LST 29 June, 1800 LST 30 June, and 1800 LST 1 July, 1800 LST 2 July, and 1800 LST 3 July. The ensemble perturbations are generated by subtracting the ensemble mean from each of the 10-member ensemble fields at these times. This results in 50 total ensemble perturbations, which are then recentered to the ERA5 reanalysis fields at 1800 LST 3 July to create the 50-member initial ensemble.

Afterward, the 50-member ensemble is integrated forward using the WRF Model until 0600 LST 4 July. This 12-h spinup process ensures a dynamically consistent background error covariance $\mathbf{P}_b$ for the subsequent DA cycles. The DA period includes 15 cycles spanning from 0600 LST 4 July to 2100 LST 4 July, with each cycle consisting of a 1-h ensemble forecast following its analysis step. During the analysis step, various observations are assimilated, including in situ surface and radiosonde data, as well as satellite-derived atmospheric motion vectors (AMVs) from the Global Telecommunications System (GTS). Additionally, all-sky upper-tropospheric water vapor channel (channel-5) BTs from the SEVIRI instrument aboard *Meteosat-8* are assimilated (Fig. 3a). To optimize the assimilation of satellite all-sky infrared radiances, adaptive observation error inflation (Minamide and Zhang 2017) and adaptive background error inflation (Minamide and Zhang 2019) techniques are applied. A fifth-order piecewise polynomial function, as defined by Gaspari and Cohn (1999), is used to localize the influence of observations on model states, reducing the impact of spurious long-distance correlations caused by the limited ensemble size. The localization settings for various observations follow those used in Hartman et al. (2023).

Following the DA period, the final ensemble analysis at 2100 LST 4 July is used to initialize the 50-member ensemble forecast, extending to 2100 LST 5 July. This forecast period encompasses the MCS initiation occurred around 0500 LST 5 July and its subsequent upscale growth (Figs. 1a–d). The final ensemble forecast will be used for further investigation.

In the 50-member ensemble forecasts, 32 members successfully capture the timing and location of MCS initiation. A forecast is considered a successful ensemble member if the predicted MCS initiation location is within 150 km and the predicted initiation timing is within 2 h of the observed initiation. Without DA (i.e., without assimilating any observations during the DA period shown in Fig. 3b), only 13 members capture the MCS initiation (not shown). This demonstrates that DA significantly improves the forecast accuracy of MCS initiation, consistent with findings by Chan et al. (2022).

4. Role of diurnal gravity waves in MCS initiation

In this section, we examine the role of diurnal gravity waves originating from the east coast of India in the initiation of offshore MCS using the ensemble forecast. The same analysis was performed across all 32 successful ensemble members, showing consistent diurnal gravity wave characteristics and similar impacts on the offshore environment. Therefore, we focus on analyzing gravity waves in one representative member, referred to as the control (CTL) member. The development of the MCS in CTL is shown in Figs. 1e–h.

While CTL overall realistically captures the initiation and upscale growth of the MCS event, one difference between CTL and observation can be noted is the presence of some spurious cold clouds over the offshore region during the early forecast hours (0300 LST, Fig. 1e). This feature is commonly observed in ensemble-based all-sky infrared radiance DA (e.g., Chan and Chen 2022; Chan et al. 2023; He et al. 2023), where the ensemble mean is calculated and updated at each analysis step. Averaging ensemble members can result in thin upper-level cold clouds in the initial condition. These clouds, unlike the forecasted MCS initiated around 0500 LST, do not produce precipitation or exhibit strong vertical motion (shown later). Hence, we expect they have a limited direct impact on the MCS initiation. Most of these spurious clouds dissipate in the following hours of the model integration (e.g., Figs. 1f–h).

We begin by examining the changes in local low-level temperature and moisture profiles prior to MCS initiation in CTL, as thermodynamic conditions are known to be critical for convective initiation (e.g., Chen et al. 2023; Schiro and Neelin 2019; Schiro et al. 2020). At 2200 LST (i.e., 7 h before MCS initiation), a dry inversion layer is present between 980 and 930 hPa at the MCS initiation location (Fig. 4a). This inversion results from leeside subsidence over the offshore region of Indian east coast, caused by southwesterly monsoonal winds interacting with mountain ranges over southern India (Fig. 2, also discussed in Peng and Chen 2023). The inversion creates a convective inhibition (CIN) of 58 J kg^{-1}. However, this subsidence inversion dissipates over the next few hours due to a rapid decrease in lower-tropospheric temperatures (Figs. 4a–c). Simultaneously, the moisture content in the lower-troposphere increases, approaching near-saturation around 0400 LST (Fig. 4c). From 2200 to 0400 LST (i.e., from 7 to 1 h before the MCS initiation), the mean temperature in the 980–930-hPa layer drops by ~2.0°C, while the mean dewpoint rises by ~4.5°C (Fig. 4d). In contrast, surface temperatures remain relatively stable. These thermodynamic changes from 2200 to 0400 LST result in a notable lowering of the surface-based LFC from 862 to 960 hPa, an increase in surface-based CAPE (from 4023 to 4692 J kg^{-1}), and the removal of surface-based CIN (from 58 to 0 J kg^{-1}). Furthermore, the increased relative humidity in the free lower troposphere by 0400 LST suggests a reduced impact of dry air entrainment on developing convection (e.g., Chen et al. 2022; Neelin et al. 2009; Schiro and Neelin 2019; Wolding et al. 2020). Overall, the thermodynamic conditions become increasingly favorable for convection between 2200 and 0400 LST.

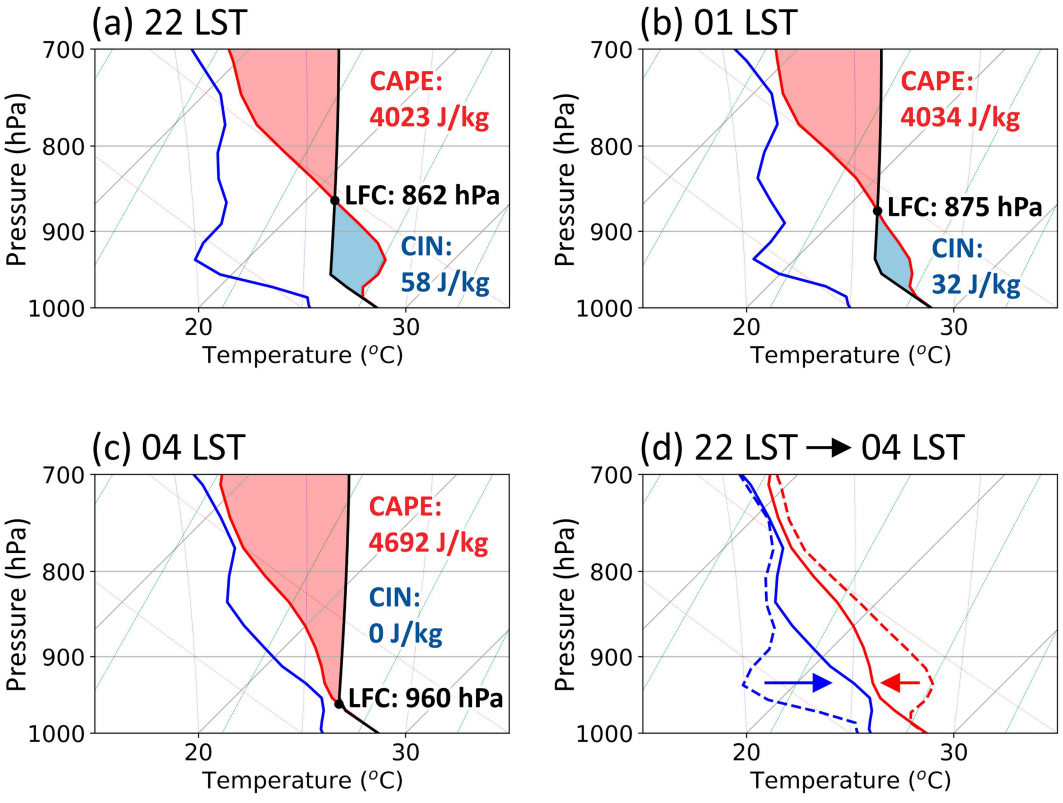

FIG. 4. Skew T–log$P$ diagrams within 25 km of the MCS initiation location in CTL at (a) 2200, (b) 0100, and (c) 0400 LST. The temperature, dewpoint, and theoretical thermodynamic path of an air parcel lifted from the surface are represented by the red, blue, and black lines, respectively. The black dot on the black line represents the LFC, and the red and blue shadings represent the CAPE and CIN, respectively. The turning point of the black line denotes lifting condensation level (LCL). The dashed lines in (d) are the same as the blue and red lines in (a), while the solid lines in (d) are the same as in (c). Other thin lines are the basic set of fixed lines that comprise the diagrams.

To determine whether the changes in offshore temperature and moisture conditions at the MCS initiation location are linked to diurnal gravity waves originating from the east coast of India, we further create an east–west cross section, 200 km in width, extending from the inland area of India to the offshore region (white arrow A in Fig. 1f). This cross-sectional analysis is used to examine the characteristics of diurnal perturbation fields (Fig. 5). Here, the diurnal perturbation of each variable is defined as the difference between the variable's value at each hour and its daily mean. The daily mean is averaged from 2100 LST 4 July to 2100 LST 5 July (the ensemble forecast period shown in Fig. 3b). To emphasize diurnal propagation signals, the diurnal perturbation fields are further adjusted by subtracting the mean diurnal perturbations averaged along the cross section, following the method of Ruppert et al. (2020).

At 2200 LST, wedge-shaped positive potential temperature perturbations develop over the offshore region of India, extending 0–400 km from the coastline, with a peak around 0.8 km in altitude (Fig. 5a). Over inland India, negative potential temperature perturbations form from the surface, driven by nighttime longwave radiative cooling. These negative perturbations extend vertically from the surface into the troposphere, exhibiting a wedge-shaped vertical structure similar to the offshore positive potential temperature perturbations (Fig. 5a). In the following hours, the potential temperature perturbation wedges propagate offshore (Figs. 5c,e).

The vertical structures and propagating characteristics of these diurnal potential temperature perturbations align with theoretical expectations of diurnal gravity waves. In linear theory, diurnal gravity waves driven by the diurnal cycle of land–sea temperature contrast appear as tilted temperature rays, with upward energy propagation along the rays (i.e., upward group velocity) and downward/offshore phase propagation (Rotunno 1983). The observed diurnal potential temperature perturbations are also consistent with diurnal gravity waves documented in previous observational (e.g., Peng and Chen 2023) and modeling (e.g., Mapes et al. 2003; Ruppert et al. 2020; Ruppert and Zhang 2019) studies. At 0.5-km height, the horizontal offshore propagation speed of the diurnal temperature perturbations is ~14 m s^{-1}, comparable to the propagation speed of diurnal gravity waves in BoB documented in Peng and Chen (2024).

In addition to the diurnal potential temperature perturbations, the diurnal moisture perturbations show similar wedge-shaped vertical structures and offshore-propagating characteristics

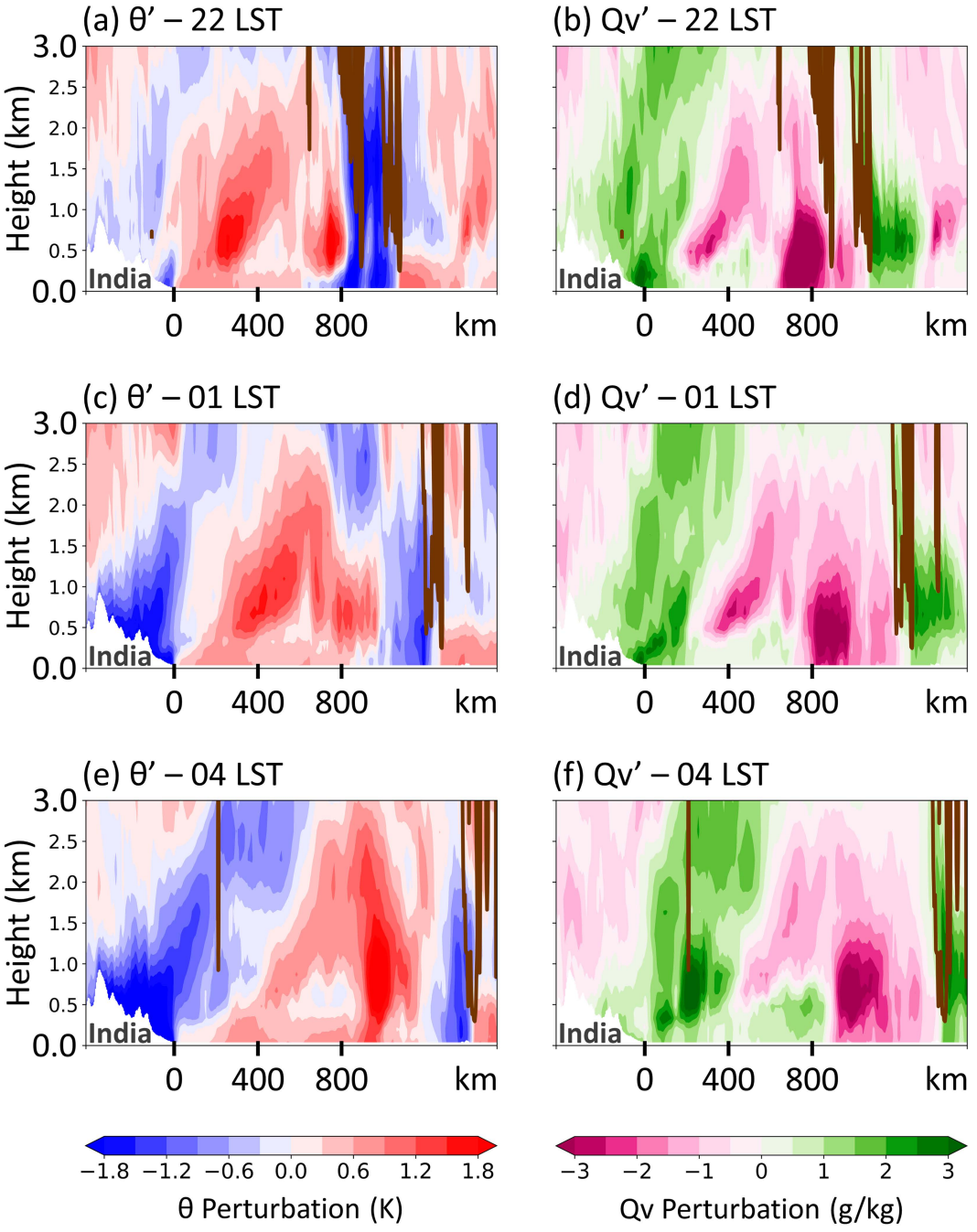

FIG. 5. Cross sections of diurnal vertical velocity (brown contour of 0.1 m s^{-1}), potential temperature θ (blue and red shadings), and water vapor mixing ratio (Qv; magenta and green shadings) perturbations along white arrow A in Fig. 1f in CTL at (a),(b) 2200, (c),(d) 0100, and (e),(f) 0400 LST. The white undulating shadings represent the topography of India. The 0 km label on the x axis indicates the location of the coastline.

(Figs. 5b,d,f). Within ~400 km from the coast, the wedge-shaped positive moisture perturbations are sandwiched between the positive potential temperature perturbation wedge to the east and the negative potential temperature perturbation wedge to the west (left and right columns of Fig. 5). The offshore propagation of positive moisture perturbations, followed by negative potential temperature perturbations, contributes to the moistening and destabilization of the offshore environment from 2200 to 0400 LST (Fig. 4), creating favorable thermodynamic conditions for the initiation of the MCS. As a result, a convective updraft begins to develop at the MCS initiation location (~200 km from the coastline) around 0400 LST (Fig. 5e).

Notably, at 2200 LST, strong convective updrafts are already present more than 800 km from the coastline (Fig. 5a). These updrafts are associated with a preexisting MCS, which weakens and moves eastward over the next few hours (Figs. 5c,e). We also examined the low-level temperature and moisture perturbations induced by this preexisting MCS and found that, due to its distance from the MCS initiation location of interest, it has a minimal impact on the initiation process. Instead, the local thermodynamic changes at the MCS initiation location are primarily driven by the offshore-propagating wedge-shaped moisture and temperature perturbations.

The next question to address is whether these wedge-shaped diurnal perturbation fields are indeed associated with diurnal gravity waves. Previous studies by Peng and Chen (2023, 2024) have shown that diurnal gravity waves over the study region have a characteristic wavelength slightly longer than 1000 km during the summer monsoon season. To isolate these long-wavelength diurnal gravity waves, we perform a Fourier decomposition along the east–west cross section (white arrow A in Fig. 1f), using a cutoff wavelength of 1000 km, following the method in Kruse and Smith (2015). The longwave signals (wavelength $\geq$ 1000 km) of diurnal potential temperature, moisture, and vertical velocity perturbations are shown in Fig. 6, while the shorter wavelength signals (wavelength $<$ 1000 km) are shown in Fig. 7.

The results in Fig. 6 closely resemble those in Fig. 5, indicating that the offshore-propagating diurnal signals from India are primarily associated with long-wavelength diurnal gravity waves (note the same color scale is used for Figs. 5 and 6). One key feature supporting this conclusion is the out-of-phase relationship between the diurnal potential temperature and vertical velocity perturbations (Figs. 6a,c,e). This out-of-phase pattern is a characteristic of gravity waves, as opposed to convective activity, which typically exhibits in-phase vertical velocity and potential temperature perturbations. The ascent associated with long-wavelength diurnal gravity waves leads to tropospheric adiabatic cooling, which is a major factor in reducing surface-based CIN and lowering the surface-based LFC at the MCS initiation location (Fig. 4). Therefore, convective initiation occurs slightly behind the ascending region of the long-wavelength diurnal gravity waves (Fig. 6e). This finding aligns with the results of Peng and Chen (2023, 2024) and further corroborates the relative positioning of convective initiation and gravity wave–induced ascent documented by Ruppert et al. (2022).

As in Fig. 5, Fig. 6 indicates moist (dry) perturbations are positioned between the cold (warm) perturbations to the west and the warm (cold) perturbations to the east. Hence, the long-wavelength moisture perturbations exhibit a high degree of spatial correlation with the long-wavelength vertical velocity perturbations (Figs. 6b,d,f), reflecting the vertical advection of moisture introduced by the diurnal gravity waves. However, the moisture changes are not only driven by the vertical velocity perturbations associated with the gravity waves from India. Enhanced moisture perturbations are observed below the gravity wave–induced vertical velocity peaks, suggesting additional processes may be at play. This question will be further explored in section 5.

In comparison with long-wavelength diurnal gravity waves, short-wavelength diurnal gravity waves are generally less pronounced (Fig. 7). The former might be caused by the large-scale land–sea thermal contrast, while the latter can be attributed to the thermal contrast by small-scale terrain (e.g., Du et al. 2024). Based on the temperature perturbations at 0.5-km height, we estimate that the horizontal phase speed of the short-wavelength diurnal gravity waves is $\sim$11 m s^{-1}, whereas that of the long-wavelength diurnal gravity waves is $\sim$17 m s^{-1}. This is because at a given frequency (i.e., diurnal), a longer wavelength results in a higher phase speed. Despite the different phase speeds, both the long and short waves destabilize the lower troposphere around 200 km from the India–BoB coast prior to the MCS initiation (causing red line changes in Fig. 4d). In addition to the temperature perturbations, moist perturbations also lead to the destabilization of the same location (causing blue line changes in Fig. 4d).

In summary, using the CTL simulation as an example, we show that diurnal gravity waves propagating from India play a key role in preconditioning the environment for offshore MCS initiation. The ascents associated with diurnal gravity waves lead to adiabatic cooling and moistening in the lower troposphere. These processes destabilize the offshore atmosphere by lowering the surface-based LFC, eliminating surface-based CIN, and mitigating the negative effects of potential dry air entrainment. Together, these factors create a favorable thermodynamic environment for MCS initiation. Compared to short-wavelength waves, long-wavelength diurnal gravity waves ($\geq$1000 km) play a more dominant role in the environmental preconditioning.

5. Other processes contributing to MCS initiation

After confirming the role of diurnal gravity waves in preconditioning the offshore environment, we now explore the following question: Why do some ensemble members fail to capture MCS initiation? Is this due to their inability to accurately simulate the diurnal gravity waves and their impact on the offshore environment, or are other factors at play? To explore this, we present the results from one of the unsuccessful members (NoCI) and compare them with CTL. We performed the same analysis across all unsuccessful members and confirmed that the results presented here are consistent and robust for the entire group.

First, we examine the changes in temperature and dewpoint profiles prior to MCS initiation in NoCI (Fig. 8). Similar to CTL, NoCI also shows a decrease in low-level temperature and an increase in low-level dewpoint at the MCS initiation location prior to the MCS initiation (Figs. 8a,c,e). These thermodynamic changes lead to a lowering of the surface-based LFC and the elimination of surface-based CIN. However, despite these favorable conditions, no MCS initiates over the offshore region in NoCI. Direct comparisons of the vertical profiles from NoCI and CTL are shown in Figs. 8b, 8d, and 8f. Interestingly, the thermodynamic conditions in both simulations are nearly identical, although the dewpoint in NoCI is slightly lower than in CTL at a few vertical layers.

The diurnal perturbation fields along the east–west cross section from India (white arrow A in Fig. 1f) in NoCI are also

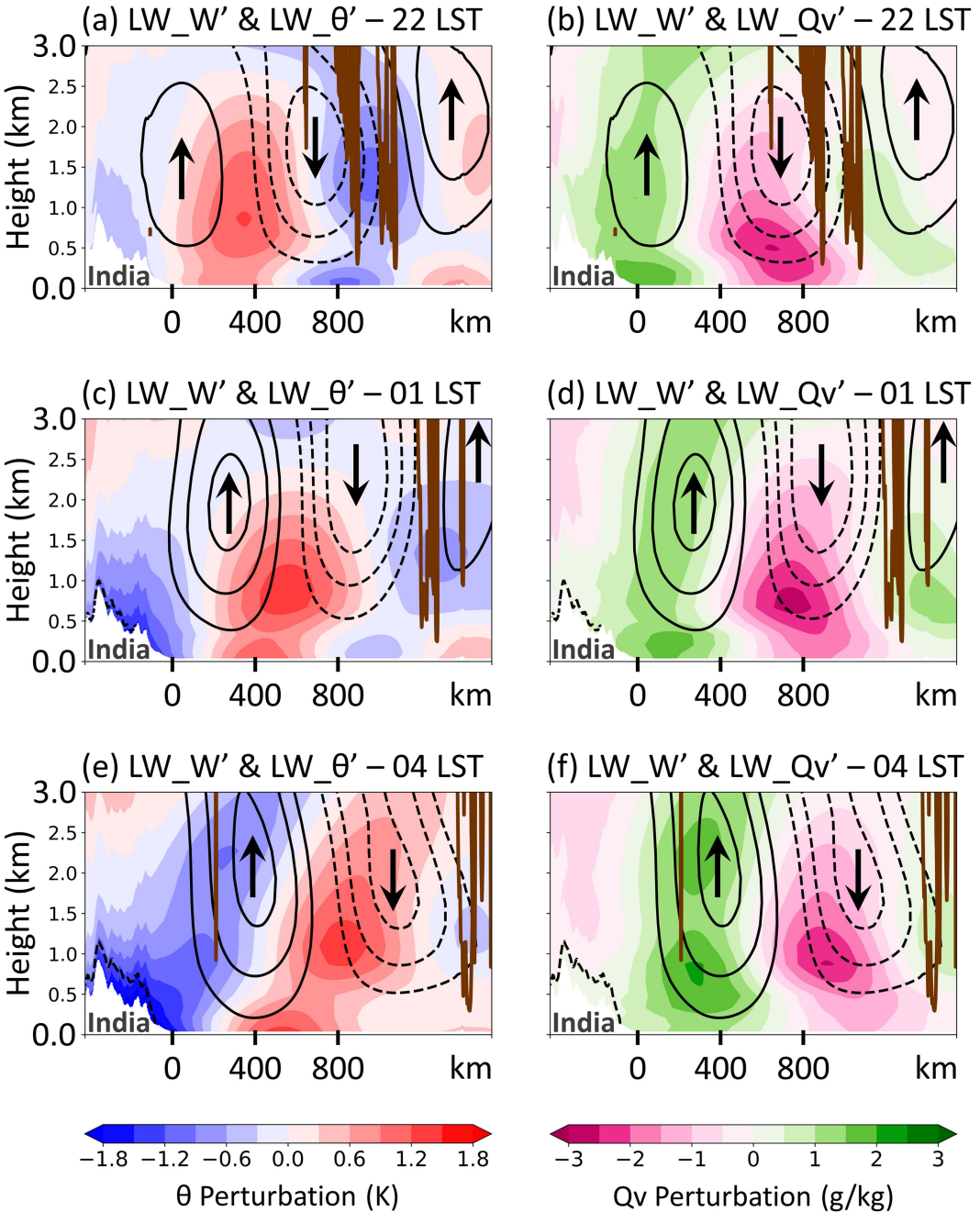

FIG. 6. As in Fig. 5, but for the LW (wavelength ≥ 1000 km) signals of diurnal vertical velocity (black contour at 0.01 m s^{-1} intervals; no zero contour), potential temperature θ (blue and red shadings), and water vapor mixing ratio (Qv; magenta and green shadings) perturbations. The up and down arrows denote the LW signals of upward and downward motions, respectively.

analyzed. The slopes, amplitudes, and propagation speeds of the temperature and moisture diurnal perturbation wedges in NoCI (Fig. 9) closely resemble those observed in CTL (Fig. 5). We also examined the long-wavelength and short-wavelength diurnal perturbations separately. The results show no significant differences from those in CTL (not shown here). These findings indicate that the diurnal gravity waves and their impacts on offshore environments are well represented even in the unsuccessful ensemble members. This suggests that other processes are responsible for the differing performance between the successful and unsuccessful members.

Besides favorable thermodynamic conditions, convective initiation also requires a mechanical triggering (i.e., lifting) mechanism. To explore whether differences in such mechanisms exist

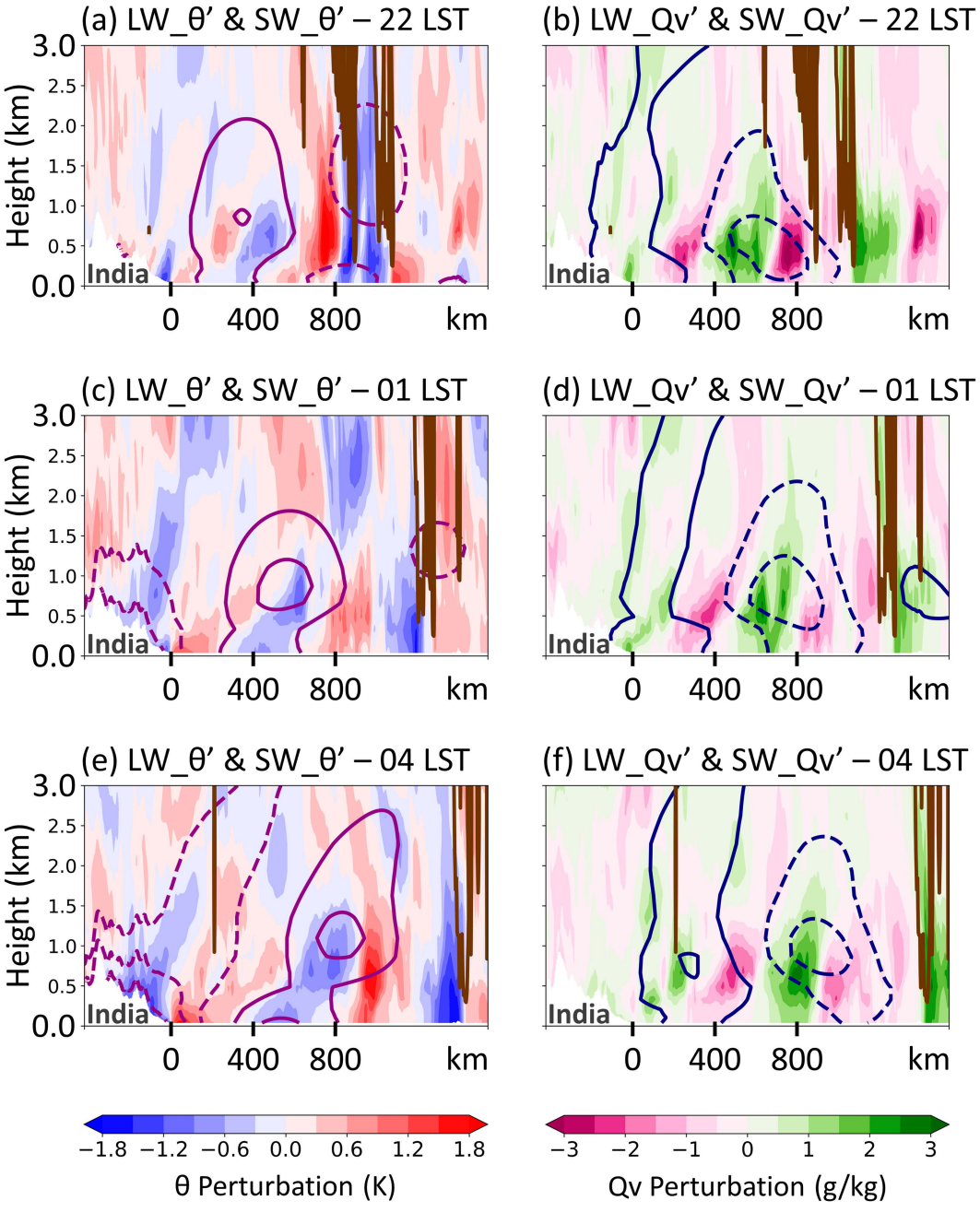

FIG. 7. As in Fig. 5, but for the LW (wavelength > 1000 km; contours at 0.6 K and 1 g kg^{-1} intervals; same as the shadings in Fig. 6) and SW (wavelength < 1000 km; color shading) signals of diurnal potential temperature θ and water vapor mixing ratio (Qv) perturbations.

between the successful and unsuccessful members, we start by comparing the temperature and moisture fields at 0.75-km height in both NoCI and CTL (Fig. 10). At this height, these fields exhibit the most pronounced changes when compared to other altitudes (Fig. 8).

Before 0500 LST, a relatively cold and moist air mass is observed south of the MCS initiation location in both NoCI and CTL (marked as "C" in Fig. 10). This air mass originates near the east coast of Sri Lanka and subsequently propagates northward to the MCS initiation location. During this process, its moisture content gradually increases. The sharp increase in boundary layer moisture near the MCS initiation location at 0400 LST, seen in Figs. 5f and 9f, corresponds with the arrival of the air mass. Since MCS initiation in CTL occurs immediately after the air mass reaches the initiation location, we hypothesize that the northward-propagating cold and moist air

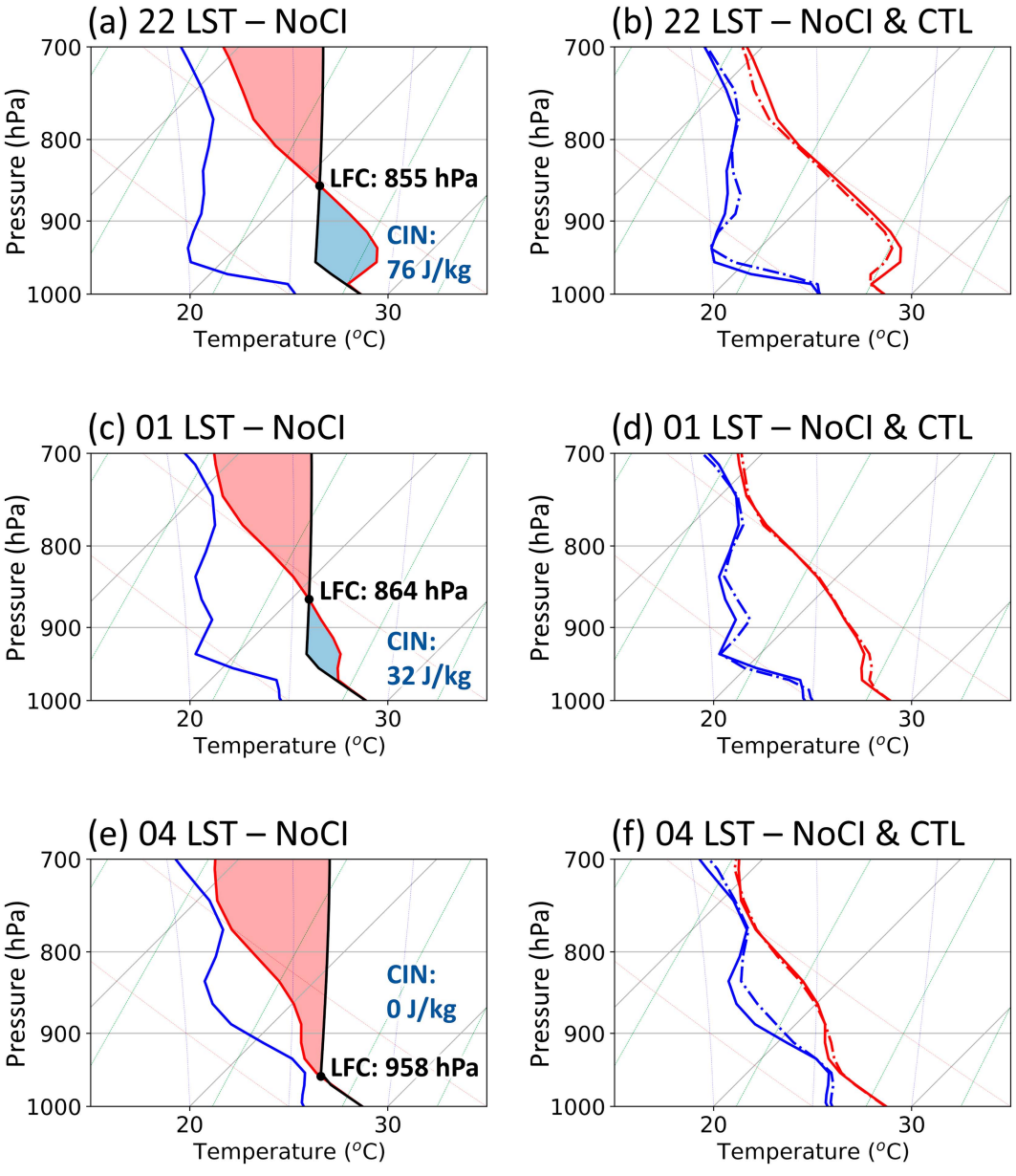

FIG. 8. As in Fig. 4, but for NoCI at (a) 2200, (c) 0100, and (e) 0400 LST. The solid lines in (b), (d), and (f) are the same as the blue and red lines in (a), (c), and (e), while the dash–dotted lines are from CTL.

from Sri Lanka may play a key role in triggering the offshore MCS initiation.

The northward-propagating signals from Sri Lanka are also evident at the surface in both NoCI and CTL (Fig. 11). These surface signals manifest as density currents due to their colder nature (marked as C in Fig. 11) than surrounding oceanic environment. These density currents are offshore-propagating land breezes, instead of cold-pool outflows from precipitation, given there is no significant nighttime rainfall over Sri Lanka (e.g., Figs. 1a,e). The land breezes travel ~300 km from the Sri Lankan coast, aided by the strong background surface monsoonal winds. Upon reaching the MCS initiation location in CTL, these land breezes trigger the MCS, which subsequently generates multiple cold pools (seen as bubble-like contours within the white boxes in Fig. 11f). In contrast, no MCS initiation occurs in NoCI at the same location (within the white boxes in Fig. 11c). Notably, the land breezes from East India do not reach CTL's MCS initiation location before 0500 LST in both NoCI and CTL. Additionally, CTL incorrectly simulates a cold-cloud convective system to the east of Sri Lanka (Fig. 1e). The convective system generates multiple local cold pools (seen as bubble-like contours ~10.00°N, 82.50°E in Fig. 11f). However, the cold-pool outflow boundaries also do not reach the MCS initiation location.

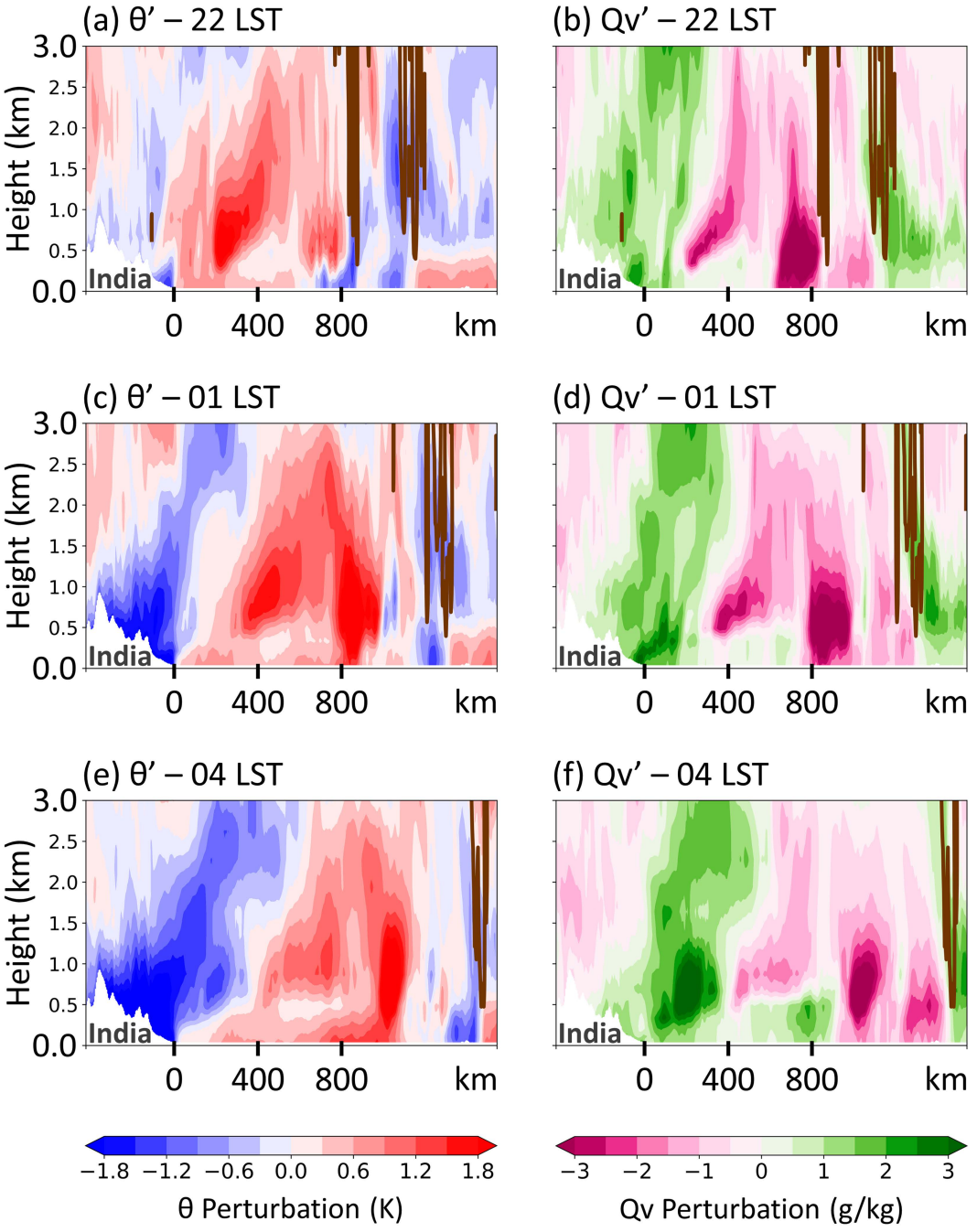

FIG. 9. As in Fig. 5, but for NoCI.

It is also noteworthy that the western BoB displays a general increase in moisture prior to the MCS initiation in both NoCI and CTL (Fig. 11, from 2300 to 0500 LST). This nocturnal moisture increase can be attributed, at least in part, to the intensification of surface monsoonal winds, which extract more moisture from the ocean (e.g., Peng and Wu 2020). The surface winds intensify in the nighttime due to the southwesterly wind enhancement induced by the diurnal gravity waves from India (Du 2023).

Figures 10 and 11 suggest that the land breezes from Sri Lanka may contribute to the MCS initiation in CTL and play a crucial role in differentiating the performance of ensemble members. To further investigate their potential influence, an additional cross section, with a width of 100 km, is created extending from northern Sri Lanka to the western BoB, passing through the MCS initiation location (white arrow B in Figs. 1f and 11f). This cross section is oriented approximately parallel to the surface and boundary layer wind directions (Figs. 10 and 11). The

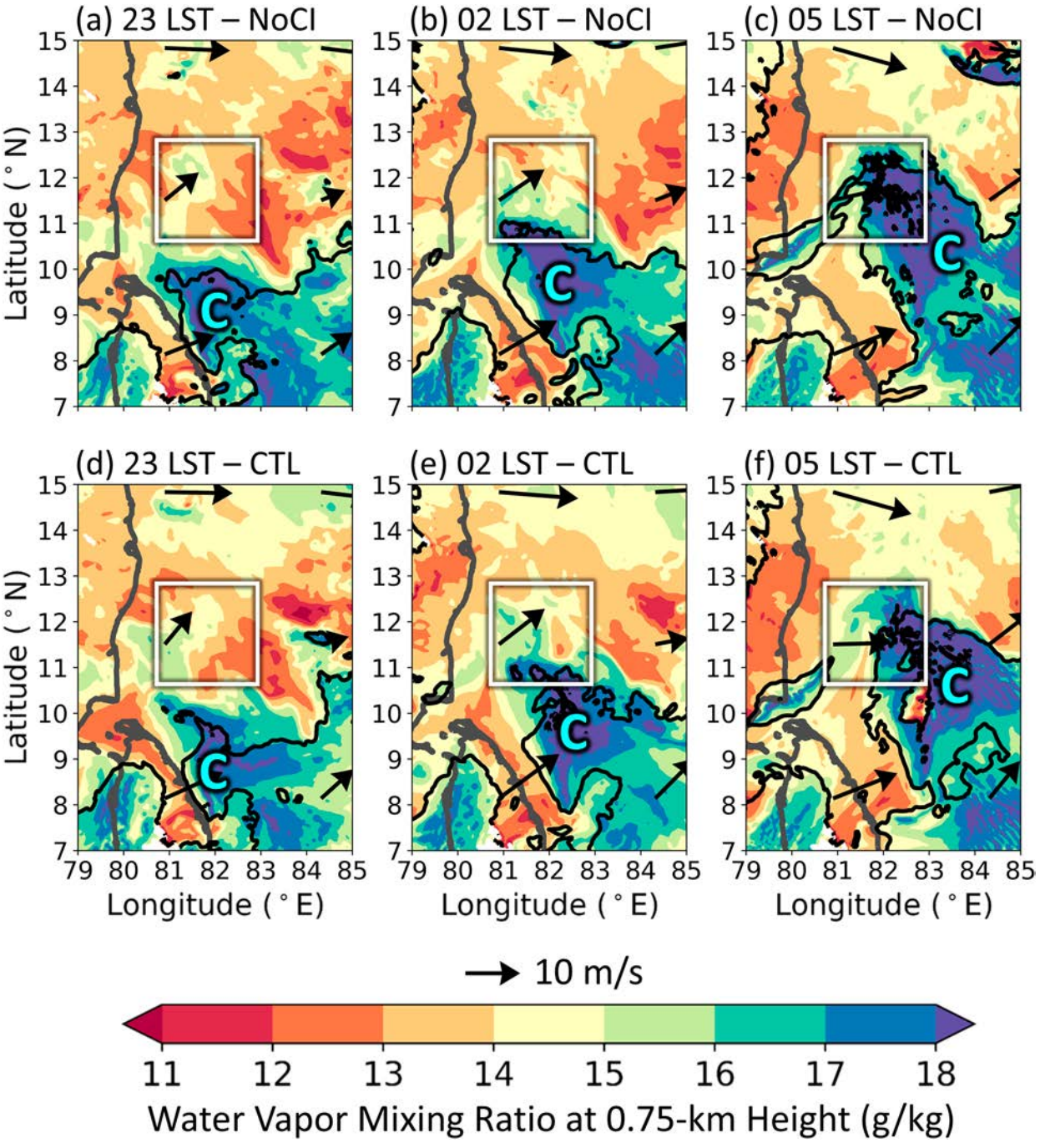

FIG. 10. Plan views of horizontal wind (vector), potential temperature (black contour of 303 K; the cold side is marked as C), and water vapor mixing ratio (shading) near the coasts of India and Sri Lanka (gray line) at 0.75-km height in NoCI at (a) 2300, (b) 0200, and (c) 0500 LST. (d)–(f) As in (a)–(c), but for CTL. The MCS in CTL initiates within the white boxes around 0500 LST.

vertical structures of offshore winds (Figs. 12–14), temperature (Fig. 12), moisture (Fig. 13), and wind divergence and surface-based LFC (Fig. 14) along the cross section from NoCI and CTL are compared to assess the role of the land breezes.

Both NoCI and CTL show that the land breezes from northern Sri Lanka, characterized by cold potential temperature and offshore wind, extend to the western BoB between 2200 and 0400 LST (Fig. 12). The offshore-propagating land breezes generate enhanced convergence at their leading edge (i.e., land-breeze front; green dots in Fig. 14), which lifts surface air and causes both adiabatic cooling and moistening in the boundary layer (Figs. 12 and 13). This process explains the

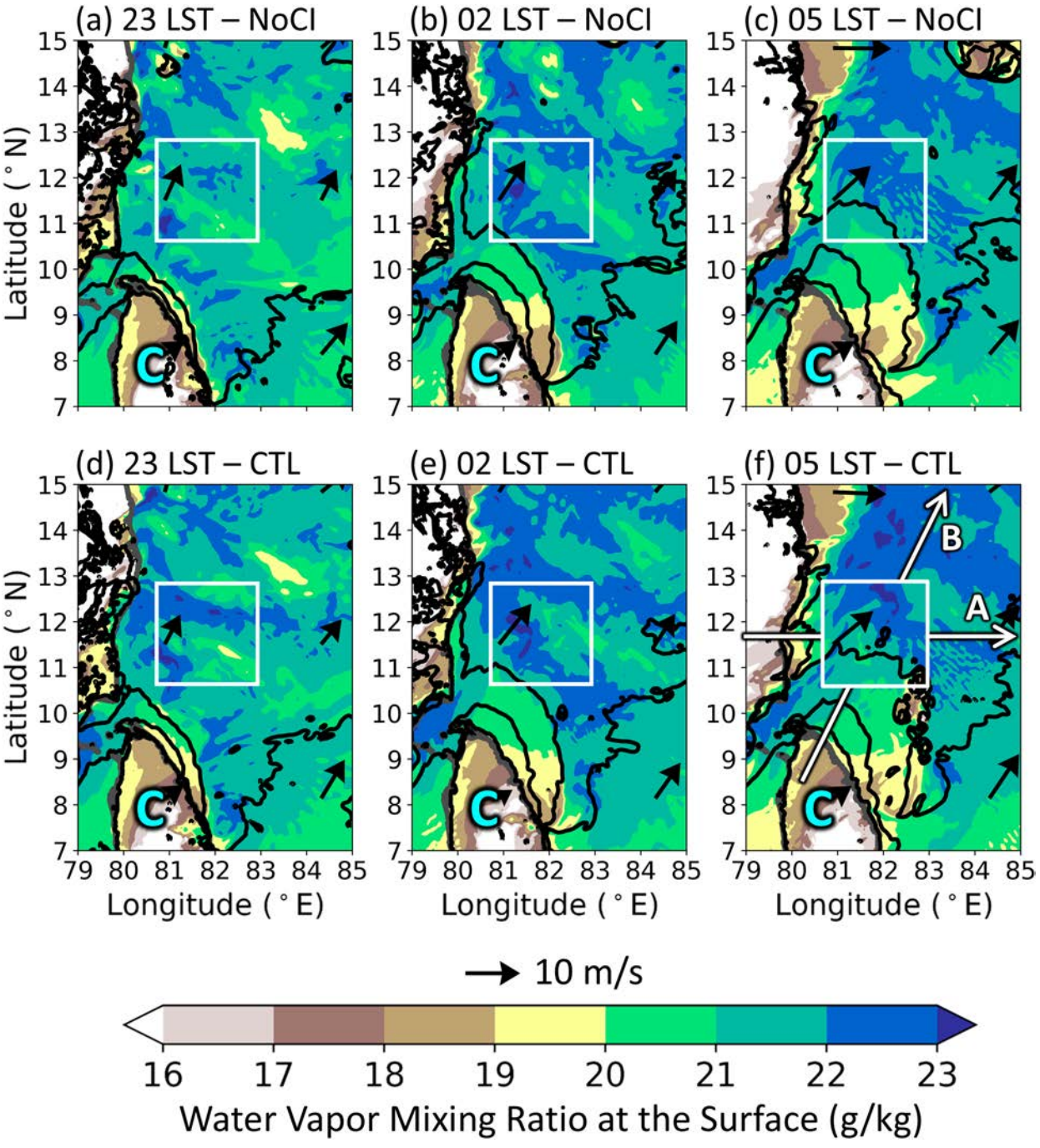

FIG. 11. As in Fig. 10, but at the surface. Only the black contours of 300, 301, and 302 K are plotted, with the cold side marked as C. White arrows A and B in (f) are the same as that in Fig. 1f.

consistent positioning of moist air mass at 0.75-km height (Fig. 10) ahead of the land breezes (Fig. 11). The lifting associated with the land-breeze front destabilizes the lower troposphere, lowering the surface-based LFC (indicated by red lines in Fig. 14) immediately behind the front. This lowered LFC moves offshore in tandem with the advancing land-breeze front.

Between 2200 and 0100 LST, both NoCI and CTL show that the land breezes and the associated frontal convergence propagate from northern Sri Lanka to the western BoB at a speed of ~11–14 m s^{-1} (Figs. 14a–d). Given the land-breeze depth of ~600 m (Fig. 12a), the potential temperatures of 303 K for the oceanic environment and 299 K for the land-breeze air mass (Fig. 12a), and the average background surface monsoonal

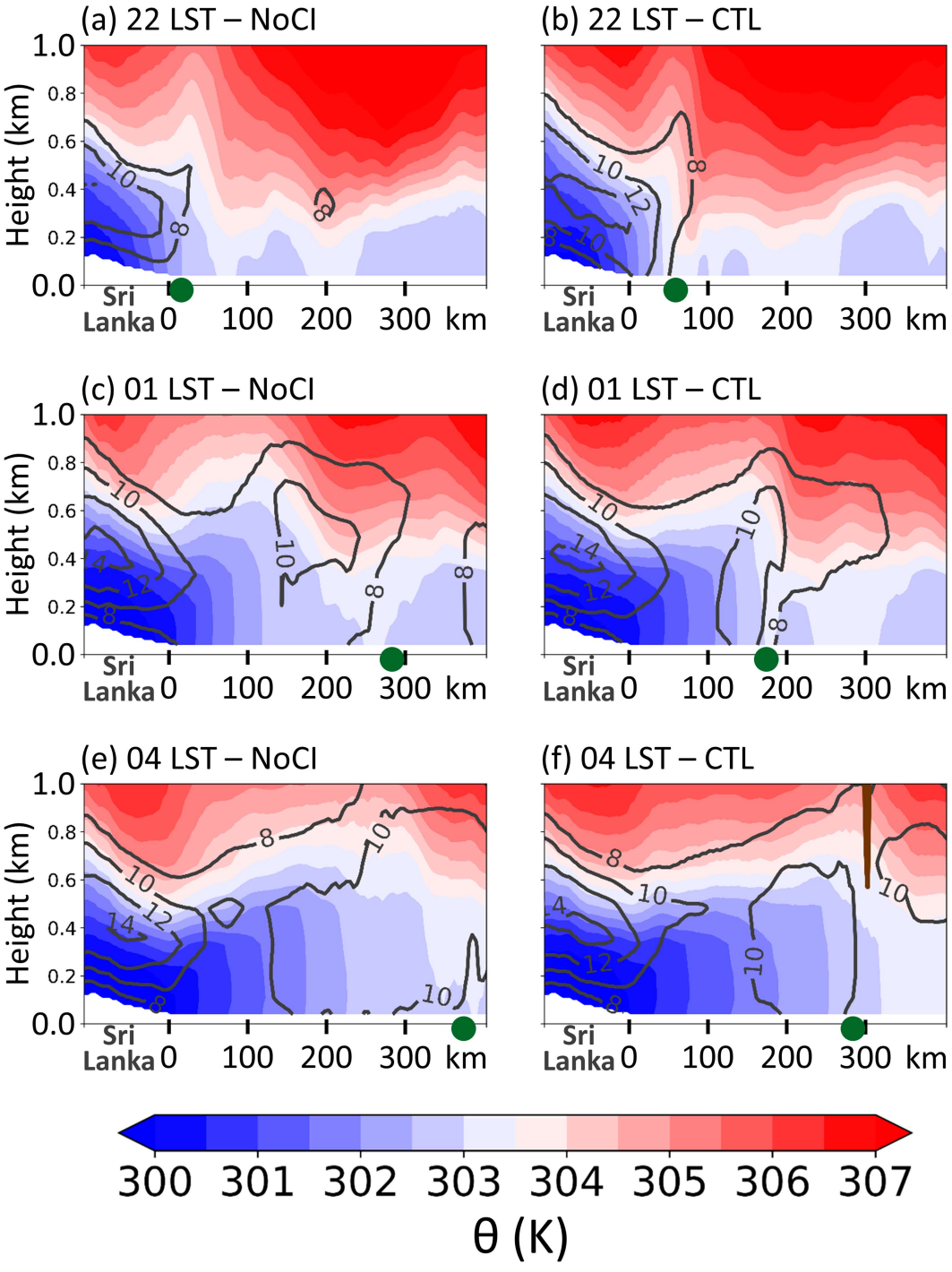

FIG. 12. Cross sections of offshore wind (gray contours), vertical velocity (brown contour of 0.1 m s^{-1}), and potential temperature (shading) along white arrow B in Fig. 11f in NoCI at (a) 2200, (c) 0100, and (e) 0400 LST. (b),(d),(f) As in (a), (c), and (e), but in CTL. The green dots indicate the leading edges of land breeze. The white undulating shadings represent the topography of northern Sri Lanka.

wind speed of 8 m s^{-1} (Fig. 11), the theoretical density current propagation speed is estimated to be ~17 m s^{-1} (Markowski and Richardson 2010). However, this theoretical speed does not account for the impacts of surface momentum and heat fluxes. According to Grant and Heever (2018), interactions between the surface and the density current can reduce the propagation speed by as much as 50%, which likely explains the slower observed speeds in the simulations.

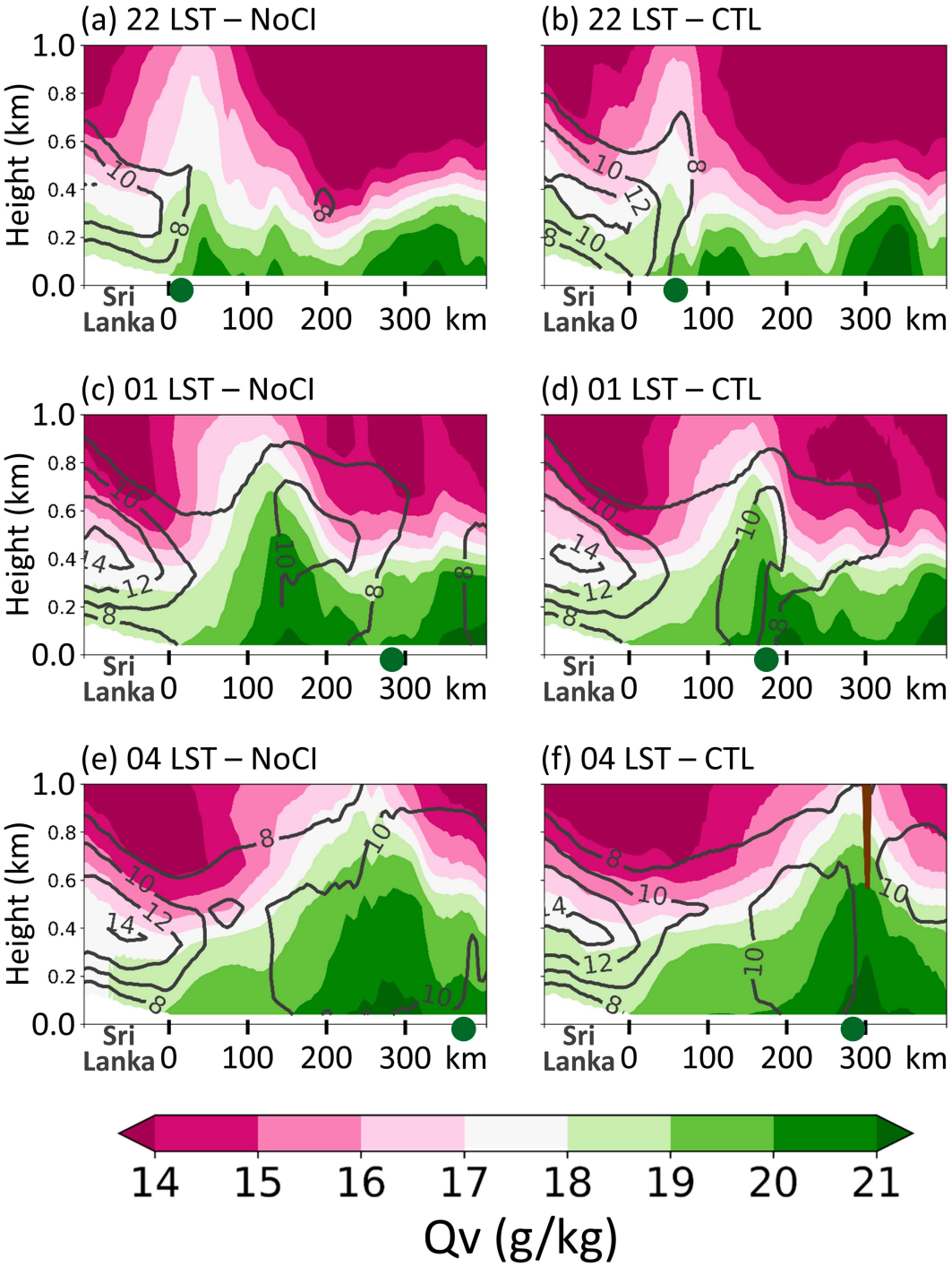

FIG. 13. As in Fig. 12, but for water vapor mixing ratio (Qv; shading).

Compared to CTL, NoCI exhibits weaker land breezes (Figs. 12–14). At 2200, 0100, and 0400 LST, the maximum offshore wind intensities associated with the land breeze in NoCI are 12.0, 14.6, and 14.3 m s^{-1}, respectively. In contrast, the corresponding values in CTL are 12.7, 14.9, and 14.8 m s^{-1}. The weaker land breezes result in weaker convergence at their leading edge (Fig. 14). From 2200 to 0400 LST, the frontal convergence in NoCI ranges from -11 to -4×10^{-5} s^{-1}, whereas in CTL, it varies from -20 to -9×10^{-5} s^{-1}. This difference in frontal convergence directly contributes to the variation in MCS initiation between NoCI and CTL. By 0400 LST, a noticeable broadening of the low-LFC region occurs in both NoCI and CTL (cf. the red lines in the third row of Fig. 14 to those in the second row). This broadening is due to the cold phase of the offshore-propagating

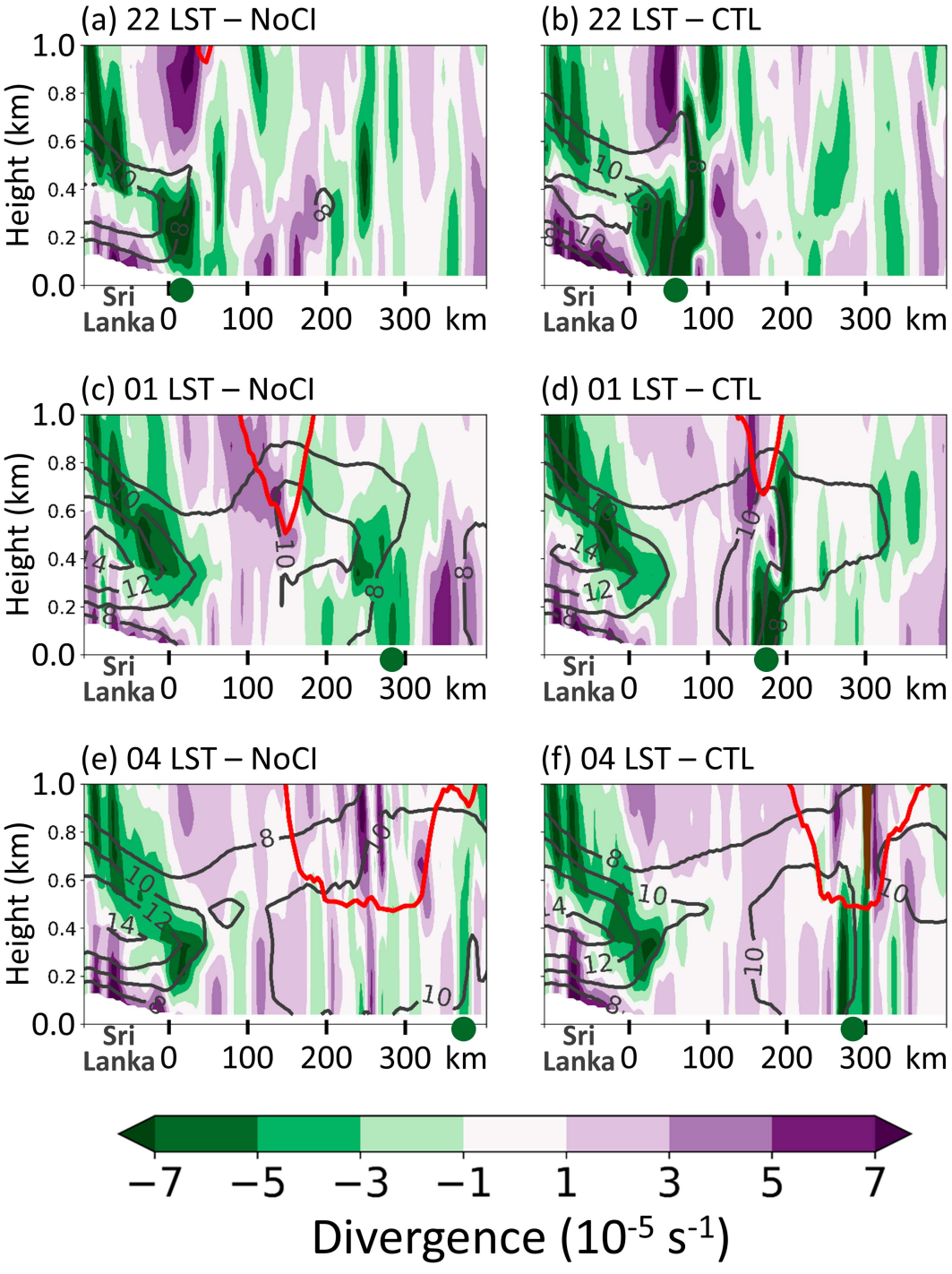

FIG. 14. As in Fig. 12, but for offshore wind divergence (shading). The red lines represent the surface-based LFCs.

diurnal gravity waves from India reaching the MCS initiation area, an effect that is visible in the cross section from northern Sri Lanka. The lowest LFCs in both NoCI and CTL are similar, consistent with the similarity in diurnal gravity waves between the two simulations (Figs. 5 and 9). In CTL, the convergence at the leading edge of the land breezes is strong by 0400 LST, and this convergence is deep enough to lift surface air above the LFC, resulting in convective initiation at approximately 300 km from the Sri Lankan coastline (Fig. 14f). However, in NoCI, the land-breeze-induced convergence is much weaker and has difficulty lifting the surface air above the LFC, thus preventing MCS initiation (Fig. 14e).

In short, while the diurnal gravity waves destabilize the lower troposphere by drastically reducing surface-based CIN

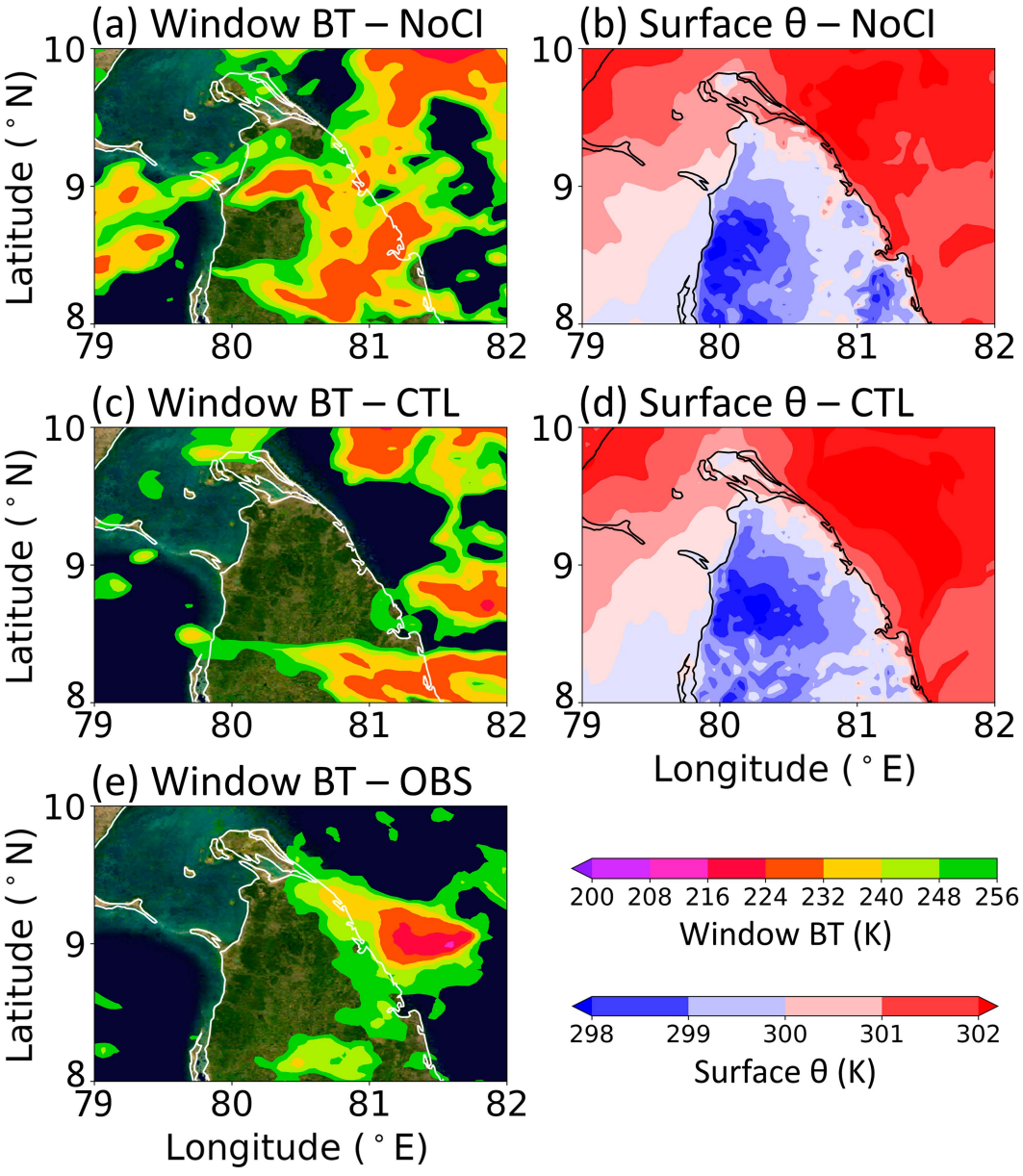

FIG. 15. Plan views of window channel BTs over northern Sri Lanka at 2100 LST from (a) NoCI, (c) CTL, and (e) *Meteosat-8* OBSs. (b),(d) As in (a) and (c), but for surface potential temperature θ.

in both CTL and NoCI, they do not necessarily initiate an MCS. Instead, the land-breeze front from northern Sri Lanka plays a critical role in triggering the MCS and differentiates the performance of CTL and NoCI. The weaker land-breeze front in NoCI can be partially attributable to the initially weaker land breeze in NoCI compared to CTL. It is because NoCI overestimates cloud cover over northern Sri Lanka, compared to both CTL and observations (Figs. 15a,c,e). Since clouds reduce longwave emission to space, there is less extended and weaker surface cooling over northern Sri Lanka in NoCI (Figs. 15b,d).

To assess whether CTL and NoCI are representatives of all successful and unsuccessful ensemble members, respectively, we analyze the relevant mesoscale processes across the entire 50-member ensemble. Figure 16a compares CIN at the observed MCS initiation location at 0400 LST between successful and unsuccessful members. The results indicate that CIN across all ensemble members ranges from 0 to 1 J kg^{-1}, suggesting that diurnal gravity waves effectively preconditioned the offshore environment in all cases. Furthermore, there is no statistically significant difference in CIN between successful and unsuccessful members, implying that gravity wave preconditioning was similar across the ensemble. In contrast, the difference in land-breeze frontal convergence at 0400 LST between successful and unsuccessful simulations is statistically significant at the 95% confidence level, with successful members

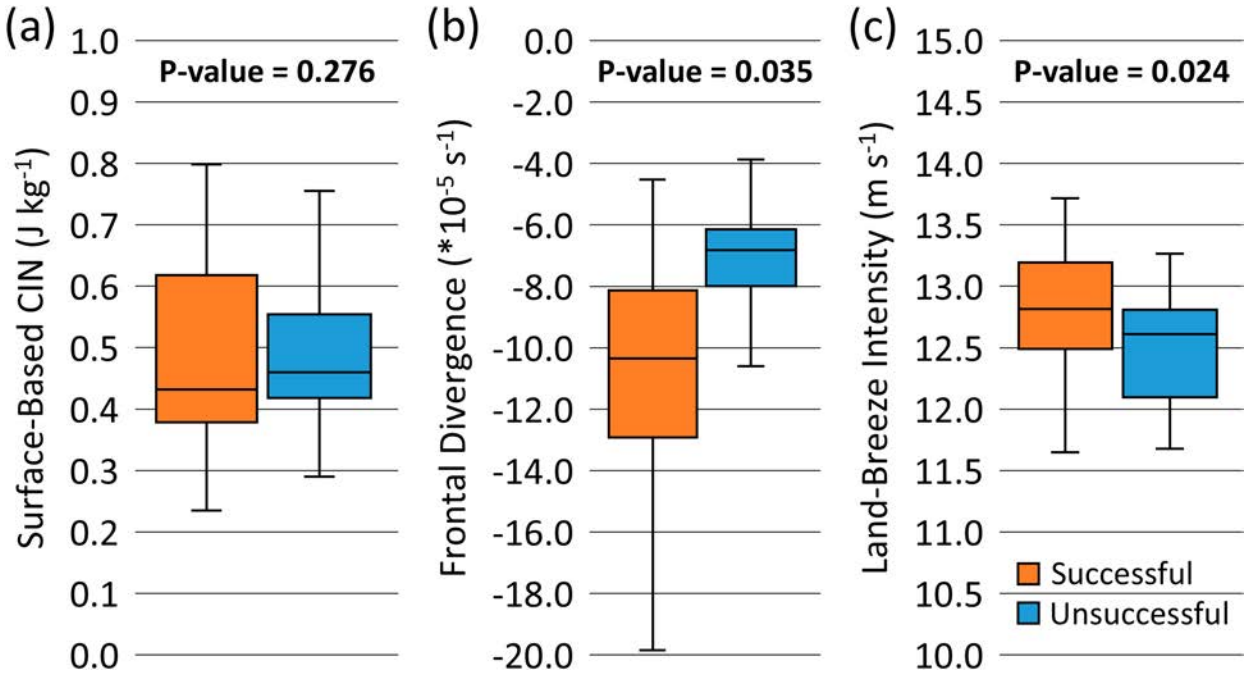

FIG. 16. (a) Surface-based CIN and (b) land-breeze frontal divergence at 0400 LST, along with (c) land-breeze intensity (defined as offshore wind speed within 200 km of the coastline) at 2100 LST, in successful (orange boxes) and unsuccessful (blue boxes) members.

exhibiting significantly stronger frontal convergence (Fig. 16b). In addition, the land-breeze intensity at forecast initialization (2100 LST) also shows a statistically significant difference between successful and unsuccessful simulations at the 95% confidence level (Fig. 16c). This trend persists when examining land-breeze intensities from 2100 to 0400 LST (not shown), further supporting our conclusion.

The improved MCS initiation forecast skill with satellite data assimilation (as mentioned in section 3b) may partly stem from better-constrained initial cloud and moisture fields through all-sky infrared radiance observations. However, how the initial cloud/moisture fields influence the practical predictability of offshore MCS initiation deserves further investigation, such as systematically modulating these initial fields, as done in Hartman et al. (2024).

6. Conclusions and discussion

In this research, we employ a convection-permitting 50-member ensemble-based satellite data assimilation experiment to investigate the roles of diurnal gravity waves and other mesoscale processes in the initiation of a typical summer monsoon MCS over the western BoB. The original objective of using the model simulations is to ascertain the underlying mechanisms responsible for the frequent MCS initiation within the low-level ascending areas of diurnal gravity waves, as indicated by Peng and Chen (2023, 2024). The result shows that the low-level ascents induced by the diurnal gravity waves from India indeed serve as convective preconditioners, causing adiabatic cooling and moistening in the lower troposphere. The processes destabilize and moisten the lower troposphere, thereby facilitating MCS initiation. Therefore, climatologically, MCSs are frequently initiated following the low-level ascending areas of diurnal gravity waves.

However, we find that diurnal gravity waves are not the sole factor contributing to MCS initiation. Our results indicate that the land-breeze front from northern Sri Lanka plays a crucial role in determining the timing and location of MCS initiation. Whether an ensemble member can successfully capture offshore MCS initiation largely depends on its ability to accurately simulate the cloud cover, surface temperature, as well as the development of land breeze over northern Sri Lanka. Thus, the practical predictability of MCS initiation heavily relies on the model's capacity to represent pre-MCS clouds and surface-to-boundary layer processes accurately. The assimilation of satellite all-sky radiances significantly enhances the prediction of offshore MCS initiation, likely because it better constrains the initial moisture and cloud fields.

In this case study, we demonstrate that the land breeze from northern Sri Lanka is a potential mesoscale trigger for offshore MCS formation. However, this does not preclude the influence of other boundary layers and/or surface processes, such as cold pools, in initiating MCSs in the region. Future investigations comparing different MCS initiation cases are warranted to better understand these contributing mechanisms. Also, we primarily focus on the mesoscale processes leading to MCS initiation (i.e., deep convective initiation) in this study. This investigation addresses some of the open questions raised in our previous papers (Peng and Chen 2023, 2024). However, the physical processes governing the upscale growth of deep convection following its initiation are equally important, remain incompletely understood, and deserve further

investigation. Our findings show that the assimilation of all-sky satellite radiance data not only enhances the forecast accuracy of MCS initiation but also improves predictions of the upscale growth of convection, compared to the experiment without data assimilation. Previous studies have suggested that a variety of environmental factors, including environmental moisture and wind shear, may influence the upscale growth of tropical MCS (e.g., Schiro et al. 2020; Chen et al. 2023). We also plan to continue utilizing these ensemble members to explore the impact of various environmental factors—such as moisture at different levels and wind shear—on the upscale growth rate of deep convection, using ensemble sensitivity analysis and sensitivity experiments.

Acknowledgments. We thank Drs. Man-Yau Chan, Ruby Leung, and Zhe Feng for their helpful discussions. We also thank the three anonymous reviewers for their constructive comments and suggestions. The authors are supported by the Office of Science of DOE Biological and Environmental Research through the Water Cycle and Climate Extremes Modeling (WACCEM) scientific focus area funded by the Regional and Global Model Analysis program area and National Oceanic and Atmospheric Administration (NOAA) under Cooperative Agreement NA24OARX459C0006 for the Consortium for Advanced Data Assimilation Research and Education (CADRE). The data assimilation experiments and ensemble forecasts were carried out using the computing resources at the National Energy Research Scientific Computing Center (NERSC), a U.S. Department of Energy Office of Science User Facility located at Lawrence Berkeley National Laboratory, operated under Contract DE-AC02-05CH11231. Data analyses were also partially carried out with the computing resources at the Texas Advanced Computing Center (TACC).

Data availability statement. ERA5 reanalyses are available at https://doi.org/10.24381/cds.bd0915c6. All assimilated GTS observations are downloaded from datasets 351.0 and 461.0 of the NCAR Research Data Archive (https://rda.ucar.edu). All assimilated *Meteosat-8* SEVIRI radiances are obtained from the EUMETSAT Data Centre (https://www.eumetsat.int/eumetsat-data-centre). PSU-EnKF analyses and WRF ensemble forecasts are archived within the Penn State Data Commons (https://doi.org/10.26208/YJ2F-A843).

REFERENCES

Bai, H., and Coauthors, 2021: Formation of nocturnal offshore rainfall near the west coast of Sumatra: Land breeze or gravity wave? *Mon. Wea. Rev.*, **149**, 715–731, https://doi.org/10.1175/MWR-D-20-0179.1.

Chan, M.-Y., and X. Chen, 2022: Improving the analyses and forecasts of a tropical squall line using upper tropospheric infrared satellite observations. *Adv. Atmos. Sci.*, **39**, 733–746, https://doi.org/10.1007/s00376-021-0449-8.

——, ——, and L. R. Leung, 2022: A high-resolution Tropical Mesoscale Convective System Reanalysis (TMeCSR). *J. Adv. Model. Earth Syst.*, **14**, e2021MS002948, https://doi.org/10.1029/2021MS002948.

——, ——, and J. L. Anderson, 2023: The potential benefits of handling mixture statistics via a bi-Gaussian EnKF: Tests with all-sky satellite infrared radiances. *J. Adv. Model. Earth Syst.*, **15**, e2022MS003357, https://doi.org/10.1029/2022MS003357.

Chen, X., K. Zhao, and M. Xue, 2014: Spatial and temporal characteristics of warm season convection over Pearl River Delta region, China, based on 3 years of operational radar data. *J. Geophys. Res. Atmos.*, **119**, 12 447–12 465, https://doi.org/10.1002/2014JD021965.

——, ——, ——, B. Zhou, X. Huang, and W. Xu, 2015: Radar-observed diurnal cycle and propagation of convection over the Pearl River Delta during Mei-Yu season. *J. Geophys. Res. Atmos.*, **120**, 12 557–12 575, https://doi.org/10.1002/2015JD023872.

——, F. Zhang, and K. Zhao, 2016: Diurnal variations of the land–sea breeze and its related precipitation over South China. *J. Atmos. Sci.*, **73**, 4793–4815, https://doi.org/10.1175/JAS-D-16-0106.1.

——, ——, and ——, 2017: Influence of monsoonal wind speed and moisture content on intensity and diurnal variations of the mei-yu season coastal rainfall over South China. *J. Atmos. Sci.*, **74**, 2835–2856, https://doi.org/10.1175/JAS-D-17-0081.1.

——, O. M. Pauluis, and F. Zhang, 2018: Regional simulation of Indian summer monsoon intraseasonal oscillations at gray-zone resolution. *Atmos. Chem. Phys.*, **18**, 1003–1022, https://doi.org/10.5194/acp-18-1003-2018.

——, L. R. Leung, Z. Feng, and Q. Yang, 2022: Precipitation-moisture coupling over tropical oceans: Sequential roles of shallow, deep, and mesoscale convective systems. *Geophys. Res. Lett.*, **49**, e2022GL097836, https://doi.org/10.1029/2022GL097836.

——, ——, ——, and ——, 2023: Environmental controls on MCS lifetime rainfall over tropical oceans. *Geophys. Res. Lett.*, **50**, e2023GL103267, https://doi.org/10.1029/2023GL103267.

Chen, Z., and Y. Du, 2024: The influence of topography on the diurnal rainfall propagation in the Bay of Bengal. *J. Atmos. Sci.*, **81**, 1019–1032, https://doi.org/10.1175/JAS-D-23-0225.1.

Chou, M.-D., and M. J. Suarez, 1999: A solar radiation parameterization for atmospheric studies. NASA Tech. Memo. NASA/TM-1999-104606, 51 pp., https://ntrs.nasa.gov/api/citations/19990060930/downloads/19990060930.pdf.

Dai, A., and K. E. Trenberth, 2004: The diurnal cycle and its depiction in the Community Climate System Model. *J. Climate*, **17**, 930–951, https://doi.org/10.1175/1520-0442(2004)017<0930:TDCAID>2.0.CO;2.

Ding, S., P. Yang, F. Weng, Q. Liu, Y. Han, P. van Delst, J. Li, and B. Baum, 2011: Validation of the community radiative transfer model. *J. Quant. Spectrosc. Radiat. Transfer*, **112**, 1050–1064, https://doi.org/10.1016/j.jqsrt.2010.11.009.

Dirmeyer, P. A., and Coauthors, 2012: Simulating the diurnal cycle of rainfall in global climate models: Resolution versus parameterization. *Climate Dyn.*, **39**, 399–418, https://doi.org/10.1007/s00382-011-1127-9.

Du, Y., 2023: Offshore migration of summer monsoon low-level jet on a diurnal scale. *Geophys. Res. Lett.*, **50**, e2023GL103840, https://doi.org/10.1029/2023GL103840.

——, R. Rotunno, Z. Chen, and H. Yang, 2024: A linear theory for periodic convectively forced gravity waves near a coastline. *J. Atmos. Sci.*, **81**, 1271–1288, https://doi.org/10.1175/JAS-D-23-0173.1.

Evensen, G., 1994: Sequential data assimilation with a nonlinear quasi-geostrophic model using Monte Carlo methods to forecast error statistics. *J. Geophys. Res.*, **99**, 10 143–10 162, https://doi.org/10.1029/94JC00572.

Fang, J., and Y. Du, 2022: A global survey of diurnal offshore propagation of rainfall. *Nat. Commun.*, **13**, 7437, https://doi.org/10.1038/s41467-022-34842-0.

Feng, Z., and Coauthors, 2021: A global high-resolution mesoscale convective system database using satellite-derived cloud tops, surface precipitation, and tracking. *J. Geophys. Res. Atmos.*, **126**, e2020JD034202, https://doi.org/10.1029/2020JD034202.

Gaspari, G., and S. E. Cohn, 1999: Construction of correlation functions in two and three dimensions. *Quart. J. Roy. Meteor. Soc.*, **125**, 723–757, https://doi.org/10.1002/qj.49712555417.

Grant, L. D., and S. C. V. D. Heever, 2018: Cold pool-land surface interactions in a dry continental environment. *J. Adv. Model. Earth Syst.*, **10**, 1513–1526, https://doi.org/10.1029/2018MS001323.

Hartman, C. M., X. Chen, and M.-Y. Chan, 2023: Improving tropical cyclogenesis forecasts of Hurricane Irma (2017) through the assimilation of all-sky infrared brightness temperatures. *Mon. Wea. Rev.*, **151**, 837–853, https://doi.org/10.1175/MWR-D-22-0196.1.

——, F. Judt, and X. Chen, 2024: Influence of local water vapor analysis uncertainty on ensemble forecasts of tropical cyclogenesis using Hurricane Irma (2017) as a testbed. *Mon. Wea. Rev.*, **152**, 1321–1338, https://doi.org/10.1175/MWR-D-23-0195.1.

He, J., X. Ma, and X. Chen, 2023: Benefit of assimilating satellite all-sky infrared radiances on the cloud and precipitation prediction of a long-lasting mesoscale convective system over the Tibetan plateau. *Quart. J. Roy. Meteor. Soc.*, **149**, 2742–2760, https://doi.org/10.1002/qj.4529.

Hersbach, H., and Coauthors, 2020: The ERA5 global reanalysis. *Quart. J. Roy. Meteor. Soc.*, **146**, 1999–2049, https://doi.org/10.1002/qj.3803.

Hong, S.-Y., Y. Noh, and J. Dudhia, 2006: A new vertical diffusion package with an explicit treatment of entrainment processes. *Mon. Wea. Rev.*, **134**, 2318–2341, https://doi.org/10.1175/MWR3199.1.

Houtekamer, P. L., and F. Zhang, 2016: Review of the ensemble Kalman filter for atmospheric data assimilation. *Mon. Wea. Rev.*, **144**, 4489–4532, https://doi.org/10.1175/MWR-D-15-0440.1.

Hu, J., and X. Chen, 2025: Mechanisms behind the long-distance diurnal offshore precipitation propagation in northwestern South America. *J. Geophys. Res. Atmos.*, **130**, e2024JD042107. https://doi.org/10.1029/2024JD042107.

Iacono, M. J., J. S. Delamere, E. J. Mlawer, M. W. Shephard, S. A. Clough, and W. D. Collins, 2008: Radiative forcing by long-lived greenhouse gases: Calculations with the AER radiative transfer models. *J. Geophys. Res.*, **113**, D13103, https://doi.org/10.1029/2008JD009944.

Jiang, Q., 2012a: A linear theory of three-dimensional land–sea breezes. *J. Atmos. Sci.*, **69**, 1890–1909, https://doi.org/10.1175/JAS-D-11-0137.1.

——, 2012b: On offshore propagating diurnal waves. *J. Atmos. Sci.*, **69**, 1562–1581, https://doi.org/10.1175/JAS-D-11-0220.1.

Kruse, C. G., and R. B. Smith, 2015: Gravity wave diagnostics and characteristics in mesoscale fields. *J. Atmos. Sci.*, **72**, 4372–4392, https://doi.org/10.1175/JAS-D-15-0079.1.

Li, Y., and R. E. Carbone, 2015: Offshore propagation of coastal precipitation. *J. Atmos. Sci.*, **72**, 4553–4568, https://doi.org/10.1175/JAS-D-15-0104.1.

Lim, K.-S. S., and S.-Y. Hong, 2010: Development of an effective double-moment cloud microphysics scheme with prognostic Cloud Condensation Nuclei (CCN) for weather and climate models. *Mon. Wea. Rev.*, **138**, 1587–1612, https://doi.org/10.1175/2009MWR2968.1.

Liu, C., M. W. Moncrieff, and J. D. Tuttle, 2008: A note on propagating rainfall episodes over the Bay of Bengal. *Quart. J. Roy. Meteor. Soc.*, **134**, 787–792, https://doi.org/10.1002/qj.246.

Mapes, B. E., T. T. Warner, and M. Xu, 2003: Diurnal patterns of rainfall in northwestern South America. Part III: Diurnal gravity waves and nocturnal convection offshore. *Mon. Wea. Rev.*, **131**, 830–844, https://doi.org/10.1175/1520-0493(2003)131<0830:DPORIN>2.0.CO;2.

Markowski, P., and Y. Richardson, 2010: *Mesoscale Meteorology in Midlatitudes*. Wiley, 432 pp., https://doi.org/10.1002/9780470682104.

Minamide, M., and F. Zhang, 2017: Adaptive observation error inflation for assimilating all-sky satellite radiance. *Mon. Wea. Rev.*, **145**, 1063–1081, https://doi.org/10.1175/MWR-D-16-0257.1.

——, and ——, 2019: An adaptive background error inflation method for assimilating all-sky radiances. *Quart. J. Roy. Meteor. Soc.*, **145**, 805–823, https://doi.org/10.1002/qj.3466.

Natoli, M. B., and E. D. Maloney, 2023: The tropical diurnal cycle under varying states of the monsoonal background wind. *J. Atmos. Sci.*, **80**, 235–258, https://doi.org/10.1175/JAS-D-22-0045.1.

Neelin, J. D., O. Peters, and K. Hales, 2009: The transition to strong convection. *J. Atmos. Sci.*, **66**, 2367–2384, https://doi.org/10.1175/2009JAS2962.1.

Peng, C.-H., and C.-C. Wu, 2020: The impact of outer-core surface heat fluxes on the convective activities and rapid intensification of tropical cyclones. *J. Atmos. Sci.*, **77**, 3907–3927, https://doi.org/10.1175/JAS-D-19-0348.1.

——, and X. Chen, 2023: Warm-season afternoon precipitation peak in the central Bay of Bengal: Process-oriented diagnostics. *J. Geophys. Res. Atmos.*, **128**, e2022JD038398, https://doi.org/10.1029/2022JD038398.

——, and ——, 2024: Monsoonal MCS initiation, rainfall, and diurnal gravity waves over the Bay of Bengal: Observation and a linear model. *J. Atmos. Sci.*, **81**, 1401–1418, https://doi.org/10.1175/JAS-D-23-0230.1.

Qian, T., C. C. Epifanio, and F. Zhang, 2009: Linear theory calculations for the sea breeze in a background wind: The equatorial case. *J. Atmos. Sci.*, **66**, 1749–1763, https://doi.org/10.1175/2008JAS2851.1.

Romatschke, U., S. Medina, and R. A. H. Houze Jr., 2010: Regional, seasonal, and diurnal variations of extreme convection in the South Asian region. *J. Climate*, **23**, 419–439, https://doi.org/10.1175/2009JCLI3140.1.

Rotunno, R., 1983: On the linear theory of the land and sea breeze. *J. Atmos. Sci.*, **40**, 1999–2009, https://doi.org/10.1175/1520-0469(1983)040<1999:OTLTOT>2.0.CO;2.

Ruppert, J. H., and F. Zhang, 2019: Diurnal forcing and phase locking of gravity waves in the maritime continent. *J. Atmos. Sci.*, **76**, 2815–2835, https://doi.org/10.1175/JAS-D-19-0061.1.

Ruppert, J. H., Jr., X. Chen, and F. Zhang, 2020: Convectively forced diurnal gravity waves in the maritime continent. *J. Atmos. Sci.*, **77**, 1119–1136, https://doi.org/10.1175/JAS-D-19-0236.1.

——, S. E. Koch, X. Chen, Y. Du, A. Seimon, Y. Q. Sun, J. Wei, and L. F. Bosart, 2022: Mesoscale gravity waves and midlatitude weather: A tribute to Fuqing Zhang. *Bull. Amer. Meteor. Soc.*, **103**, E129–E156, https://doi.org/10.1175/BAMS-D-20-0005.1.

Schiro, K. A., and J. D. Neelin, 2019: Deep convective organization, moisture vertical structure, and convective transition using deep-inflow mixing. *J. Atmos. Sci.*, **76**, 965–987, https://doi.org/10.1175/JAS-D-18-0122.1.

——, S. C. Sullivan, Y.-H. Kuo, H. Su, P. Gentine, G. S. Elsaesser, J. H. Jiang, and J. D. Neelin, 2020: Environmental controls on tropical mesoscale convective system precipitation intensity. *J. Atmos. Sci.*, **77**, 4233–4249, https://doi.org/10.1175/JAS-D-20-0111.1.

Skamarock, W. C., and Coauthors, 2019: A description of the Advanced Research WRF version 4. NCAR Tech. Note, 142 pp., https://doi.org/10.6084/m9.figshare.7369994.v4.

Tewari, M., and Coauthors, 2004: Implementation and verification of the unified NOAH land surface model in the WRF model. *20th Conf. on Weather Analysis and Forecasting/16th Conf. on Numerical Weather Prediction*. Seattle, WA, Amer. Meteor. Soc., 14.2a, https://ams.confex.com/ams/pdfpapers/69061.pdf.

Wang, C., X. Chen, K. Zhao, and C.-H. Peng, 2024: Synoptic control on the initiation and rainfall characteristics of warm-season MCSs over the South China coast. *J. Geophys. Res. Atmos.*, **129**, e2023JD039232, https://doi.org/10.1029/2023JD039232.

Wapler, K., and T. P. Lane, 2012: A case of offshore convective initiation by interacting land breezes near Darwin, Australia. *Meteor. Atmos. Phys.*, **115**, 123–137, https://doi.org/10.1007/s00703-011-0180-6.

Wolding, B., J. Dias, G. Kiladis, F. Ahmed, S. W. Powell, E. Maloney, and M. Branson, 2020: Interactions between moisture and tropical convection. Part I: The coevolution of moisture and convection. *J. Atmos. Sci.*, **77**, 1783–1799, https://doi.org/10.1175/JAS-D-19-0225.1.

Yang, G.-Y., and J. Slingo, 2001: The diurnal cycle in the tropics. *Mon. Wea. Rev.*, **129**, 784–801, https://doi.org/10.1175/1520-0493(2001)129<0784:TDCITT>2.0.CO;2.

Zhang, F., C. Snyder, and J. Sun, 2004: Impacts of initial estimate and observation availability on convective-scale data assimilation with an ensemble Kalman filter. *Mon. Wea. Rev.*, **132**, 1238–1253, https://doi.org/10.1175/1520-0493(2004)132<1238:IOIEAO>2.0.CO;2.

Zipser, E. J., D. J. Cecil, C. Liu, S. W. Nesbitt, and D. P. Yorty, 2006: Where are the most intense thunderstorms on Earth? *Bull. Amer. Meteor. Soc.*, **87**, 1057–1072, https://doi.org/10.1175/BAMS-87-8-1057.

Zuidema, P., 2003: Convective clouds over the Bay of Bengal. *Mon. Wea. Rev.*, **131**, 780–798, https://doi.org/10.1175/1520-0493(2003)131<0780:CCOTBO>2.0.CO;2.